SATB1 undergoes isoform-specific phase transitions in T cells

Tomas Zelenka[1,2], Petros Tzerpos[1,3], Giorgos Panagopoulos[4], Konstantinos C. Tsolis[2], Dionysios-Alexandros Papamatheakis[1,2], Vassilis M. Papadakis[2], David Stanek[5], Charalampos Spilianakis[1,2,#]

[1] Department of Biology, University of Crete, GR70013 Heraklion, Crete, Greece

[2] Institute of Molecular Biology and Biotechnology—Foundation for Research and Technology Hellas, GR70013 Heraklion, Crete, Greece

[3] Department of Biochemistry and Molecular Biology, Faculty of Medicine, University of Debrecen, Debrecen, HU-4032 Hungary (current address)

[4] Biomedical Research Foundation, Academy of Athens, 4 Soranou Efessiou Street, Athens 11527, Greece

[5] Institute of Molecular Genetics of the Czech Academy of Sciences, Prague, Czech Republic

[#] Corresponding author, email: spiliana@imbb.forth.gr

Abstract

Intracellular space is demarcated into membraneless bodies and compartments via the process of liquid-liquid phase separation (LLPS). Phase separated condensates formed by proteins, RNA and/or other biomolecules are associated with many cellular functions including gene expression regulation. Here we describe how the genome organizer SATB1 utilizes its prion-like domains for LLPS. We have identified two SATB1 isoforms which display distinct biophysical behavior. We further showed how phosphorylation and interaction with nuclear RNA impact their phase transitions, leading to formation of aggregates when dysregulated. Moreover, we show that SATB1 is involved in the regulation of transcription and splicing, both of which displayed deregulation in *Satb1* knockout murine thymocytes. Thus, the tight regulation of different SATB1 isoform expression levels, combined with protein post-translational modifications, are imperative for SATB1's physiological roles in T cell development while their deregulation may be linked to disorders such as cancer.

Keywords: SATB1, phase separation, prion, PrLD, poly-Q, T cells, thymocytes, nuclear matrix, chromatin organization, immunity, cancer.

Introduction

Phase transition of biomolecules into liquid-like condensates is an important mechanism of intracellular organization and it was proposed to regulate many cellular processes[1]. The ability of a protein to undergo LLPS depends on its structure together with environmental cues. LLPS is mostly driven by weak multivalent interactions between the protein's intrinsically disordered regions (IDRs) and is often accompanied by interactions with RNA[2,3]. Low-complexity prion-like domains (PrLDs) and RNA binding domains are known features that affect a protein's biophysical properties[4,5]. Glutamine-rich proteins and proteins harboring a poly-Q domain also display prion-like characteristics[6]. Moreover, proteins with poly-Q domains and/or PrLDs are known to undergo LLPS[4,5,7–10]. However, such proteins are also prone to abnormalities and their phase transitions frequently result in fibrous amyloids or other rigid aggregates, which are associated to several pathologies[8,11]. Despite often having negative connotation, PrLDs most certainly play some important physiological roles; from regulating the solubility of proteins, to processes linked to LLPS, such as gene expression regulation and others[12].

In general, the regulatory mechanisms of protein's phase transitions into liquid-like condensates and/or solid aggregates are poorly understood. There are several contributing factors including post-translational modifications and alternative splicing[13]. The latter is gaining attention as a robust tissue-specific regulatory mechanism of gene expression, allowing the production of functionally diverse proteins from a single gene[14]. More specifically, alternative splicing allows subtle changes to LLPS propensity as well as more dramatic inclusion or exclusion of whole IDRs or other regions, defining a protein's LLPS properties. A regulatory role of alternative splicing in LLPS has already been described for BRD4[15], TAU[16,17], hnRNPDL[18] and other proteins,

collectively constituting examples of distinct mechanisms on how alternative splicing affects LLPS[13].

Recently, we have investigated the function of the poly-Q and PrLD-containing protein SATB1 as a mediator of the 3D enhancer network in developing T cells[19]. In this work, we focus on the physiological and pathological implications of SATB1's phase transitions. Apart from its physiological roles in T cells, where it is predominantly expressed[20], SATB1 has been largely studied in the context of various cancers[21–23]. Besides its function as a tissue-specific genome organizer[19,24], it also modulates nuclear architecture by recruiting chromatin modifying protein complexes[25,26]. The properties of individual SATB1 domains were recently characterized *in vitro*, in cell lines[27]. Here, we utilized primary murine T cells, in which we have identified two full-length SATB1 protein isoforms. These isoforms display different biophysical properties, further emphasizing the importance of alternative splicing, as an additional regulatory layer for T cell development. Both SATB1 isoforms bear two PrLDs and a short poly-Q domain, collectively providing a LLPS potential to SATB1. We showed that the interaction with RNA controls SATB1's localization in the nucleus. Moreover, SATB1's phosphorylation in the serine residue S635 regulated its phase transitions and DNA binding ability. Consistent with its phase separating properties, SATB1 was involved in transcription and splicing processes and its mislocalization to cytoplasm resulted in protein aggregation. The deregulated production of the two SATB1 isoforms and their altered phase transitions resulting in protein aggregation can contribute to the severity of pathologies such as cancer.

Results

Identification of a novel SATB1 protein isoform

SATB1 protein consists of an N-terminal part containing the ULD (ubiquitin-like oligomerization domain; similar in sequence to the PDZ domain) and CUTL (CUT repeat-like) domains which are responsible for its self-oligomerization[27–30] and the interaction with other proteins[25,26,31]. The CUT1, CUT2 domains and a homeodomain are responsible for SATB1's DNA binding activity and are all localized to its C-terminus (Fig. 1a). Between CUT2 and the homeodomain, there is a glutamine-rich region following the predicted extra peptide (EP) of the long SATB1 isoform [UniProt: long SATB1 isoform E9PVB7_Mouse (795 aa), short SATB1 isoform Q60611 (764 aa)]. In this work, we performed stranded-total-RNA-seq experiments in murine thymocytes to identify the existing *Satb1* transcripts. We detected about 5.6-fold enrichment of the transcripts encoding the short (764 amino acids) over the long (795 amino acids) *Satb1* isoform (Fig. 1b). Note also the presence of seven additional annotated transcripts, three of which may encode for truncated protein isoforms and four untranslated transcripts (do not contain an open reading frame, ORF) which all may have an unknown regulatory function. To validate these findings, we designed primers for RT-qPCR experiments in a way that the forward primer either hybridized at the 3'-end of exon10 and simultaneously at the 5'-end of exon11 (Fwd1) or entirely within the extra exon (Fwd2) of the long isoform, to specifically amplify either the short or the long *Satb1* transcripts, respectively (Fig. 1c). We confirmed that in murine thymocytes the steady state mRNA levels of the short *Satb1* transcripts were about 3-5 fold more abundant compared to the steady state mRNA levels of the long *Satb1* transcripts (Fig. 1d). To validate the existence of the long SATB1 isoform, we generated a custom-made antibody specifically targeting the extra peptide of 31 amino acids originating from the extra *Satb1* exon (Fig. 1a). Moreover, we also developed an antibody targeting the native form of the N-terminal part of SATB1 (the first 330 amino acid residues; Fig. 1a). None of the commercially available antibodies can distinguish between the two SATB1 isoforms *in vivo*, as

they target parts of SATB1 shared by both isoforms. It should also be noted that when investigating the SATB1 protein levels, we have to bear in mind that the antibodies targeting the N-terminus of SATB1 protein cannot discriminate between the short and long isoforms, thus we can only compare the amount of the long SATB1 isoform to the total SATB1 protein levels. To overcome this limitation and to specifically validate the presence of the long SATB1 protein isoform (which would hardly be distinguishable from the short isoform based on size), we designed a serial immunodepletion-based experiment (Fig. 1e). This experiment showed, that the antibody raised against the extra peptide of the long SATB1 isoform specifically detects only the long SATB1 isoform (Fig. 1f; upper panel, lane 2) and not the short SATB1 isoform (Fig. 1f; upper panel, lane 3). The long and short SATB1 isoforms were expressed at equimolar protein levels in thymocytes (as deduced by the SATB1 signals detected by anti-SATB1 antibodies detecting both isoforms (Fig. 1f; lower panel, lanes 2 and 3). An additional validation of the specificity of the custom-made SATB1 antibody is also available (Supplementary Fig. 1a), alongside with confocal microscopy images demonstrating the extensive colocalization of SATB1 isoforms detected by both types of antibodies (Supplementary Fig. 1b). Based on this data, we concluded that in murine thymocytes a long SATB1 isoform is expressed at both mRNA and protein levels.

SATB1 is a nuclear protein and, utilizing confocal microscopy, it was previously shown to display a cage-like pattern in murine thymocytes[26]. We revisited this question and employed super-resolution microscopy approaches to study SATB1's subnuclear localization. Our results indicated that the previously described cage-like pattern of SATB1[26] at high resolution rather resembled individual speckles which may or may not be interconnected (Fig. 1g; note that the samples were fixed which may affect the shape of the observed speckles). An apparent emerging question, upon

detection of these SATB1 speckles, was whether they are involved in the regulation of physiological processes such as transcription.

SATB1 co-localizes with sites of active transcription

Each super-resolution microscopy approach comes with certain limitations, hence for our applications we compared the results from STED (Stimulated Emission Depletion; provides high resolution, lower risk of bleed-through) with 3D-SIM (3D Structured Illumination Microscopy; allows higher throughput, broader variety of fluorophores and DAPI staining, less photobleaching). In search for functional differences between the two SATB1 isoforms, we probed their subnuclear localization *in vivo*, utilizing 3D-SIM super-resolution microscopy (Fig. 2a). The quantification of SATB1 speckles in four nuclear zones, derived based on the relative intensity of DAPI staining, highlighted the localization of SATB1 mainly to the regions with medium to low DAPI staining, apparently correlated with euchromatin and interchromatin regions (zones 3 & 4, Fig. 2a, b). A similar distribution of the SATB1 signal could also be seen from the fluorocytogram of the pixel-based colocalization analysis between the SATB1 and DAPI signals (Supplementary Fig. 1c). The major difference between the localization of the different SATB1 isoforms, uncovered by the use of the two different antibodies, relied in the heterochromatin areas (zone 1), where the long isoform was less frequently present. Given the localization of SATB1 to the nuclear zones with estimated transcriptional activity (Fig. 2b, zone 3), we investigated the potential association between SATB1 and transcription. We unraveled the localization of SATB1 isoforms and the sites of active transcription labeled with 5-fluorouridine, using both STED (Fig. 2c) and 3D-SIM (Supplementary Fig. 1d). Based on qualitative evaluation (quantified in Fig. 3e) we found that the SATB1 signal was found in close proximity to nascent transcripts.

We further performed co-immunoprecipitation experiments (utilizing an antibody targeting all SATB1 protein isoforms) coupled to mass spectrometry analysis (IP-MS) to determine SATB1's interactome in murine thymocytes (Supplementary Fig. 2a-b; Supplementary File 1). Unbiased k-means clustering of the significantly enriched SATB1 interactors revealed two major clusters consisting mostly of proteins involved in transcription (blue cluster 1; Fig. 2d and Supplementary Fig. 2c) and splicing (yellow cluster 2; Fig. 2d and Supplementary Fig. 2c). Both transcription and splicing were also significantly enriched terms in the gene ontology enrichment analysis of SATB1 interactors (Fig. 2e; Supplementary File 2), indicating that SATB1 plays an important role in thymocyte RNA production and processing.

To further investigate the functional link between SATB1 and gene transcription and splicing, we performed stranded-total-RNA-seq experiments in wild type (WT) and *Satb1*$^{fl/fl}$*Cd4*-Cre^{+} (*Satb1* cKO) murine thymocytes, with SATB1 being specifically depleted at the CD4^{+}CD8^{+} T cells during thymocyte development[19]. Consistent with SATB1's localization at transcription sites, we identified a vast deregulation with 1,641 (922 down-regulated, 719 up-regulated) differentially expressed genes (Fig. 2f) and 2,014 genes with altered splicing efficiency (Supplementary Fig. 2d-e; Supplementary File 3-4). We should note that the extent of deregulation of spliced genes was directly correlated to SATB1 binding (Supplementary Fig. 2d; SATB1 binding sites identified in our manuscript; GSE173446[19]). Similarly, the transcription of multiple genes was directly affected by SATB1 binding as we previously demonstrated[19].

In summary, we found that in the primary thymocyte nucleus, SATB1 localized in the euchromatin and interchromatin regions in close proximity to actively transcribed genes, interacted with protein complexes involved in the regulation of gene transcription and mRNA splicing and upon *Satb1* deletion, both physiological processes of transcription and splicing were deregulated.

SATB1 protein is phase separated *in vivo*

SATB1 has a predicted phase separation potential[5]. Here we demonstrated its connection to transcription and found that it forms almost perfectly spherical speckles (Fig. 1g), markedly resembling phase separated transcriptional condensates[32,33]. Thus, we next investigated whether the observed nuclear SATB1 speckles could be a result of LLPS. To probe differences in phase separation in mouse primary cells, without any intervention to SATB1 structure and expression, we first utilized 1,6-hexanediol treatment, which was previously shown to dissolve the liquid-like droplets[34]. If SATB1 was indeed undergoing LLPS into the transcriptional condensates, we would expect to detect a sensitivity of the SATB1 speckles to the hexanediol treatment, followed by decreased colocalization with fluorouridine-labeled sites of active transcription. The long SATB1 isoform speckles evinced such sensitivity as demonstrated by a titration series with increasing concentrations of 1,6-hexanediol treatment followed by 3D-SIM super-resolution microscopy analysis (Fig. 3a-b; note the log scale). Moreover, analysis with STED microscopy revealed that the long SATB1 isoform was more sensitive to hexanediol than collectively all SATB1 protein isoforms (Fig. 3c). Additionally, hexanediol treatment highly decreased colocalization between SATB1 and fluorouridine-labeled sites of active transcription (Fig. 3d). To quantify the difference in colocalization between SATB1 and fluorouridine-labeled sites of active transcription, as well as the changes upon hexanediol treatment, we used a pixel-based colocalization analysis (Fig. 3e and Supplementary Fig. 3a-c). Based on these results, the long SATB1 isoform displayed a higher association with sites of active transcription and this association was more sensitive to the hexanediol treatment than collectively all SATB1 isoforms.

To expand our study regarding the effect of 1,6-hexanediol in dissociating SATB1 speckles, we employed Raman spectroscopy, a non-invasive label-free approach, which is able to detect changes in chemical bonding. Raman spectroscopy was already used to predict global

transcriptomic profiles from living cells[35], thus we reasoned that it may also be used to study phase separation. We measured Raman spectra in primary thymocytes derived from both WT and *Satb1* cKO animals and compared them with spectra from cells upon 1,6-hexanediol treatment. Principal component analysis of the resulting Raman spectra clustered the treated and non-treated *Satb1* cKO cells together, while the WT cells clustered separately (Fig. 3f). The WT 1,6-hexanediol treated cells clustered between the aforementioned groups. These results suggested that the principal component 1 (PC1) could discriminate WT and *Satb1* cKO cells based on chemical bonding provided by SATB1 protein. These bonds were probably enriched for weak interactions responsible for LLPS that are susceptible to hexanediol treatment. This shifted the cluster of WT treated cells towards the *Satb1* cKO cells. However, the remaining covalent bonds differentiated the WT samples from *Satb1* cKO cells where all bonds provided by SATB1 were absent. This approach demonstrated that Raman spectroscopy can be utilized as a non-invasive research approach to unravel the global chemical state of a cell and its changes upon various conditions. Moreover, together with the light microscopy experiments, it allowed us to investigate SATB1's biophysical behavior *in vivo*.

The N-terminus of SATB1 undergoes LLPS

To further support our findings that SATB1 undergoes LLPS, we utilized the light-inducible CRY2-mCherry optoDroplet system[36] (Fig. 4a). This tool allows studying the phase separating properties of individual parts of a protein in a controlled manner. The CRY2-mCherry chimeric constructs, encoding part of a protein of interest are transiently transfected into cells. Following illumination by high energy light, the photo-responsive CRY2 protein is induced to homo-oligomerize while bringing the protein molecules of interest into spatial proximity. Only proteins with phase separating properties will then form droplets, which are visualized by accumulation of

the mCherry signal. First, we selected the multivalent N-terminal part of SATB1 (1-298 aa), which is known for its involvement in protein-protein interactions[25,26,28–31]. Note, that the multivalent nature of a protein indicates its predisposition to undergo LLPS[1–3]. Moreover, the selected region of SATB1 includes part of a prion-like domain (Fig. 4a), which makes the N-terminus of SATB1 a prospective candidate with LLPS potential. Live transfected NIH-3T3 cells were activated with a 488 nm laser, every two seconds, to initiate CRY2 association and mCherry signal was detected. For the analysis, cells were grouped into two categories based on the original mCherry relative fluorescence, reflecting the transfection efficiency, as this directly affects the speed of droplet assembly[36]. The construct encompassing the N-terminus of SATB1 formed optoDroplets at a similar or even faster rate than the FUS positive control (Fig. 4b, live videos in Supplementary File 5), a popular model for LLPS studies[36]. The low SATB1 concentration group of cells evinced the first optoDroplets ~10 seconds upon induction, compared to FUS, where the first optoDroplets appeared after ~14-20 seconds upon stimulation. Cells with higher SATB1 expression levels displayed even faster optoDroplet assembly, where both FUS and the N-terminus of SATB1 started forming optoDroplets at ~6 seconds upon activation. The formed speckles resembled phase separated droplets based on their round shape and ability to fuse (Fig. 4c and Supplementary Fig. 4a). The droplet assembly rate for both the N-terminal part of SATB1 and FUS proteins (Fig. 4d), highlighted the direct correlation between protein concentration and the speed of droplet assembly. We detected a higher number of FUS optoDroplets that were formed, however the N-terminus SATB1 optoDroplets grew in bigger sizes (Fig. 4b and Supplementary Fig. 4b). FUS optoDroplets disassembled entirely after 100 and 250 seconds of inactivation time (488 nm laser off), for the low and high protein expression groups, respectively. In contrary, the optoDroplets formed by the N-terminus of SATB1 displayed a much slower disassembly rate and often even after ten minutes

of inactivation time there were some rigid structures still present (Fig. 4e). The group of cells with a lower concentration of the SATB1 N-terminus displayed a gradual decrease in droplet size during inactivation time, unlike the high concentration group (Supplementary Fig. 4c). Considering the original faster assembly of SATB1 droplets, we hypothesized that they also turned more quickly into long-lasting aggregates, which would also explain the differences between the low and high concentration group of cells. This was also in line with the decreased circularity of droplets from the high concentration group compared to the low concentration samples (Supplementary Fig. 4a). Moreover, the FRAP experiments indicated that SATB1 droplets had around 43% of an immobile fraction compared to FUS with only 17% of an immobile fraction (Fig. 4f). However, the mobile fraction of SATB1 droplets manifested a halftime of recovery 3.3 seconds, much lower than the halftime of 11.4 seconds of FUS droplets, supporting the hypothesis that the N-terminus constructs were generally over-activated.

The N-terminus of SATB1 is shared by both the short and long SATB1 isoforms, so with the use of the optoDroplet system we investigated whether the two full length SATB1 isoforms could undergo LLPS similar to the shorter N-terminal part. Upon activation, both full-length isoforms displayed visible ultrastructural changes which were reversible upon inactivation (Fig. 5a). However, these did not resemble the optoDroplets detected for FUS and the N-terminus of SATB1, as deduced from the number and size of the optoDroplets detected (Supplementary Fig. 4d-e). Although the full length SATB1 bears a nuclear localization signal (aa 20-40), we identified a fraction of cells where the protein was localized in the cytoplasm, in a form of rigid aggregates (Fig. 5b). Computational analysis, using the algorithm *cat*GRANULE[37], of the protein sequence for both murine SATB1 isoforms indicated a higher propensity of the long SATB1 isoform to undergo LLPS with a propensity score of 0.390, compared to 0.379 for the short isoform (Fig. 5c).

This difference was dependent on the extra peptide of the long isoform. Out of the 31 amino acids comprising the murine extra peptide, there are six prolines, five serines and three glycines – all of which contribute to the low complexity of the polypeptide region[3]. Note also the higher LLPS propensity of the human long SATB1 isoform compared to the murine SATB1 (Fig. 5c). Since cytoplasmic protein aggregation has been previously described for proteins containing poly-Q domains and PrLDs, we next generated truncated SATB1 constructs encoding two of its IDR regions, the poly-Q domain and in the case of the long SATB1 isoform also the extra peptide neighboring the poly-Q domain (Fig. 1a and 4a). The constructs containing the extra peptide of the long SATB1 isoform frequently resulted in protein aggregates which did not respond to CRY2 activation (Fig. 5d). The constructs derived from the short SATB1 isoform did not form almost any aggregates or only in a very small fraction of cells (Fig. 5d). These results support the difference in the biophysical behavior of the two SATB1 isoforms.

Modes of regulation of SATB1 phase transitions

To determine why SATB1 forms aggregates in the cytoplasm, we next investigated the potential means of regulation for the SATB1 phase transitions. Phase separating properties of prion-like proteins are regulated by the presence of nuclear RNA, which keeps them in a soluble form when in the nucleus[38]. However, currently it is not known whether SATB1 interacts with RNA at all. The data presented here involve SATB1 to both transcription and splicing (Fig. 2 and 3). Moreover, SATB1 was originally discovered as a protein of the nuclear matrix[39], where RNA represents one of its main components and thus implying that SATB1's association with RNA is plausible. To test this hypothesis, we performed nuclear matrix extraction experiments, including RNase A treatment, to investigate the potential association of SATB1 with RNA. A fraction of SATB1 remained in the nucleus even after the extraction of cells with high concentrations of salt or treatment with DNase I,

though the treatment with RNase A alone depleted SATB1 from the cell nucleus of murine thymocytes (Fig. 6a). One of the prominent RNAs associated with the nuclear matrix is lncRNA Xist, whose interaction with SATB1 was already predicted[40]. To further validate these findings, we performed RNA immunoprecipitation experiments utilizing antibodies against the SATB1 protein and we detected the association between SATB1 and Xist lncRNA (Fig. 6b). Moreover, when we forced localization of the long SATB1 isoform IDR constructs to the nucleus, by fusing them to the SV40 nuclear localization signal, the protein signal remained diffused in the cell nucleus (Fig. 6c) and notably it did not respond to the CRY2 activation even after 20 minutes of activation. Therefore, here we demonstrated that SATB1 in primary murine T cells is capable of association with RNA, that its localization in the nucleus is highly dependent on the presence of nuclear RNA and that the nuclear environment affects phase transitions of SATB1.

Another factor affecting the phase transitions of proteins includes their post-translational modifications. More specifically, the phosphorylation of the PrLD of FUS protein was shown to prevent its aggregation[41,42]. Similarly, the efficient disassembly of stress granules and other membraneless organelles was dependent on phosphorylation[43–45]. SATB1 harbors many verified and predicted phosphorylation sites[20]. The selected IDR region of SATB1 (Fig. 4a) contains multiple serine residues which are targets of phosphorylation. Based on DNA affinity chromatography coupled to mass spectrometry, we identified a novel SATB1 phosphorylation site, S635 (S666 in the long isoform, Supplementary Fig. 5a). To investigate the impact of phosphorylation in position S635, which directly follows the PrLD, we generated a S635A SATB1 mutant, abolishing phosphorylation at this site (Fig. 4a). We performed DNA affinity purification assays, utilizing protein extracts from transiently transfected cells (no endogenous SATB1 expressed) with either the wild type or mutated SATB1 and found that this mutant had abrogated

DNA binding ability (Supplementary Fig. 5b). Even more importantly, a CRY2-mCherry construct with the mutated part (S635A) of the short SATB1 isoform developed aggregates in the cytoplasm (Fig. 6d), similar to those of the cytoplasmic long isoform (Fig. 5d). This observation suggested that phosphorylation of SATB1 plays an important role in its phase transitions, affecting DNA binding and the potential regulatory effects of SATB1 on genome organization and transcriptional gene regulation.

Furthermore, a regulatory mechanism coordinating the production of the short and long *Satb1* isoforms could also control SATB1's phase transitions – given their differential LLPS propensity. Such a mechanism could rely on the differential promoter usage as recently reported[46,47]. Our stranded-total-RNA-seq experiments revealed a series of long isoform transcripts originating from various *Satb1* promoters, though indistinguishable from promoters priming the short isoforms (Fig. 6e). Therefore, we reasoned that a more plausible hypothesis would be based on the regulation of alternative splicing. We should note that we have identified a binding site specific to the long SATB1 isoform[19] (right at the extra exon of the long isoform; Fig. 6e), suggesting a potential autoregulatory role for the expression of the long SATB1 isoform. The study of alternative splicing based on our RNA-seq analysis revealed a deregulation in the usage of the extra exon of the long *Satb1* isoform (the only *Satb1* exon affected) in *Satb1* cKO cells (deltaPsi = 0.12, probability = 0.974; Supplementary File 4), further suggesting that SATB1 itself is able to control the levels of the short and long *Satb1* isoforms. A possible mechanism controlling alternative splicing is based on its kinetic coupling with transcription. Several studies indicated how histone acetylation and generally increased chromatin accessibility may lead to exon skipping, due to enhanced RNA polymerase II elongation[48,49]. We hypothesized that the regulation of *Satb1* gene may include similar mechanisms, possibly even being regulated by a negative feedback loop

via the long SATB1 isoform binding, resulting in increased chromatin accessibility at the extra exon and thus exon skipping. This hypothesis is supported by the increased usage of the extra exon in the absence of SATB1 in *Satb1* cKO (Supplementary File 4). To further address this, we utilized the TCGA breast cancer dataset (BRCA) as a cell type expressing SATB1[50]. ATAC-seq experiments for a series of human patients with aggressive breast cancer[51] revealed differences in chromatin accessibility at the extra exon of the *SATB1* gene (data not shown), suggesting its potential involvement in alternative splicing regulation according to the "kinetic coupling" model. Indeed, the increased chromatin accessibility at the extra exon (allowing faster read-through by RNA polymerase) was positively correlated with the expression of the short *SATB1* isoform and slightly negatively correlated with the long *SATB1* isoform (Fig. 6f). Moreover, we investigated whether the differential expression of *SATB1* isoforms was associated with poor disease prognosis. Worse pathological stages of breast cancer and expression of *SATB1* isoforms displayed a positive correlation for the long isoform but not for the short isoform (Fig. 6g and Supplementary Fig. 5c). This was further supported by worse survival of patients with increased levels of long *SATB1* isoform and low levels of estrogen receptor (Supplementary Fig. 5d). These observations not only supported the existence of the long *SATB1* isoform in humans, but they also shed light at the potential link between the regulation of *SATB1* isoforms production and their involvement in pathological conditions.

Discussion

In this work we described the existence of two SATB1 protein isoforms in both human and mouse and investigated their biophysical properties. We demonstrated that SATB1 in primary murine thymocytes was mainly localized in the transcriptionally active nuclear zone and co-localized with sites of active transcription. Unfortunately, we could not directly compare differences between the

long and short SATB1 isoforms *in vivo*. However, the long SATB1 isoform-specific speckles evinced higher colocalization with fluorouridine-labeled sites of active transcription as well as higher sensitivity to hexanediol, compared to the speckles detected by antibodies targeting collectively all SATB1 isoforms. Following these observations, we can hypothesize that in primary murine thymocytes the long SATB1 isoform was more frequently phase separated and thus also associated active transcription and splicing.

Furthermore, we used a heterologous system with genetically engineered optogenetic constructs to investigate the biophysical properties of different SATB1 polypeptides. The N-terminus of SATB1, shared by both SATB1 isoforms, displayed rapid LLPS in the CRY2-mCherry optoDroplet system. We analyzed transiently transfected cells, separately, based on the relative recombinant protein concentration. Notably the low-expressing cells transfected with the N-terminus of SATB1 displayed even faster droplet assembly compared to the positive control FUS. Correspondingly, in the highly-expressing cells, SATB1 tended to form larger structures, generally displaying signs of over-saturation and thus conversion into gel-like or solid-like structures[1], known for PrLD proteins. Our current approach could not clearly discriminate whether overexpression, turning SATB1 into long-lasting aggregates, was solely due to the internal properties of SATB1 or due to the artificial multivalency provided by the CRY2 optogenetic system. SATB1 contains two PrLD regions, one of which is included at the 3' end of the SATB1 N-terminal construct. This PrLD also likely facilitated the LLPS of the N-terminus SATB1 optoDroplet constructs. The second PrLD directly extends the region harboring the extra peptide of the long SATB1 isoform, which by itself contributed to the slightly higher LLPS propensity of the long isoform and its aggregation in the cytoplasm. However, the forced nuclear localization of the second PrLD with the extra peptide of the long isoform, even at very high concentrations, did

not indicate any optoDroplet formation. This would suggest that the N-terminal part of SATB1 with its ability to form multivalent interactions was necessary for SATB1's LLPS. Therefore, there is only a subtle difference in the biophysical properties of the short and long SATB1 isoforms permitting the tight regulation of SATB1's biophysical behavior.

There may exist several means of regulation of SATB1's phase transitions. We showed that the nuclear RNA environment contributes to the solubility of nuclear SATB1, resulting in protein aggregation when mislocalized into the cytoplasm. Apart from nuclear RNA, buffering a protein's phase transitions[38], two studies described the role of nuclear-import receptors in chaperoning and disaggregating aberrant phases of PrLD containing proteins[52,53]. The latter does not seem to apply to SATB1, as SATB1 possesses a unique NLS lacking the clusters of basic residues, thus being dissimilar to known nuclear localization signals. This suggests that there might be other factors involved in its nuclear transport machinery[54]. Moreover, we described a novel phosphorylation site (S635) in murine SATB1 protein. The mutation S635A resulted in SATB1's aggregation and abruption of its DNA binding ability. Thus, it is reasonable to hypothesize that phosphorylation is also crucial for SATB1's interactions with RNA. SATB1 is the substrate for a great number of post-translational modifications[20], hence they likely serve important roles in the regulation of physiological processes, including the modulation of phase transitions. A functional association between SATB1 and PML bodies was already described in Jurkat cells[55]. We should note that PML bodies represent another example of phase separated nuclear bodies[56] associated with SATB1. Targeting of SATB1 into PML bodies depends on its phosphorylation status; when phosphorylated it remains diffused, whereas unphosphorylated SATB1 is localized to PML bodies[57]. This is in line with the phase separation model as well as with our results from S635A mutated SATB1, which has a phosphorylation blockade promoting its phase transitions and inducing aggregation.

There is an increasing body of evidence that PrLDs could serve important biological functions such as regulation of a protein's LLPS behavior[12]. The predicted saturation concentration (i.e. the concentration threshold that has to be crossed to trigger phase separation) of human SATB1 is 114 μM, which falls at the lower end of identified proteins with phase separation potential[5]. However, the low saturation concentration would allow a precise regulation of SATB1's LLPS just by modulating its expression levels. Moreover, given the slightly different biophysical properties of the two SATB1 isoforms, the controlled production of either the short or the long SATB1 isoform would establish yet another layer of regulation. We have recently described the SATB1-mediated promoter-enhancer network which controls the expression of important master regulator genes in developing T cells[19]. Here we hypothesize, that the increasing protein levels of SATB1 and/or the long-to-short isoform ratio could promote the incorporation of the regulated genes into the transcriptional condensates, as it was also described for other factors[58–60]. Therefore, SATB1 could be a great example where LLPS is utilized for its gene expression regulation properties. Such a mechanism of action would only be possible in primary cell types with high SATB1 concentration, such as in murine $CD4^+CD8^+$ double positive T cells or possibly in embryonic stem cells and some neurons. Moreover, the chromatin epigenetic landscape could represent another regulatory layer affecting the relative isoform abundance.

Overall, our observations set a new ground for future research as the biophysical properties of SATB1 may determine its pathological behavior in a number of disorders. Deregulation of any of the described mechanisms, such as the altered RNA binding capacity of SATB1, deregulation of its multivalency by mutations or by post-translational modifications, deregulation of its expression levels, or changes to the epigenetic landscape, ultimately leading to a different proportion of the long and short SATB1 isoforms, could all result in physiological aberrations.

Future studies should draw their attention to isoform-specific expression levels of SATB1, ideally coupled with microscopy, to reveal its localization pattern in cells. This is particularly important given the higher LLPS propensity of the human long SATB1 isoform compared to the murine SATB1 (Fig. 5c). Therefore, human cells could be more susceptible to the formation of aggregated SATB1 structures which could be associated with physiological defects. In line with our findings, there was a recent publication associating nuclear SATB1 with favorable cancer patient survival, whereas cytoplasmic SATB1 was associated with poor prognosis[61]. Moreover, there is a large knowledge gap in the identification and validation of post-translational modifications of SATB1 and their underlying function. Here we provided experimental proof for RNA binding by SATB1, however it is not yet clear which domain is capable for RNA binding and under which circumstances. Lastly, more focus should be brought to potential mutations in the susceptible poly-Q region of SATB1. Mutations of the poly-Q region may be difficult to identify, however they could lead to the extension of the poly-Q stretch, ultimately facilitating aggregate formation and thus a pathological situation as known for other PrLD-bearing proteins[8,62].

Author contributions

T.Z. and C.S. designed the study. T.Z. cloned the CRY2 constructs and transfected the cells, performed the microscopy experiments, RNA-seq experiments and the computational analyses. P.T. created the *Satb1* cKO mouse, cloned the original *Satb1* transcripts and generated custom-made antibodies. G.P. performed the SATB1 co-immunoprecipitation and mass spectrometry experiments. K.C.T. analyzed the mass spectrometry data. D.A.P. performed the immunodepletion and western blot experiments. V.M.P. performed and analyzed the Raman spectroscopy experiments. D.S. provided resources for the super-resolution microscopy and consulted the imaging experiments and the analysis for alternative splicing. T.Z. wrote the original manuscript. C.S. supervised the work, obtained funding and corrected the manuscript. All authors read, discussed and approved the manuscript.

Declaration of interests

The authors declare no competing interests.

Data availability

RNA-seq experiments and SATB1 binding sites are deposited in Gene Expression Omnibus database under accession number GSE173470 and GSE173446, respectively. The other datasets generated and/or analyzed during the current study are available upon request.

Material and methods

Animals and isolation of thymocytes

All experiments were conducted in accordance with the Laboratory Animal Care and Ethics Committee of IMBB-FORTH. Animal work was approved by the IMBB Institutional Animal Care and Ethics Committee. All the experiments were performed on mice with C57BL/6 background. The generation and validation of *Satb1*$^{fl/fl}$*Cd4*-Cre^{+} mouse was previously described[19]. The animals used for the experiments were 4-8 weeks old. Primary thymocytes were resuspended by rubbing and passing the thymus through a 40 µm cell strainer (Falcon, 352340) in 1× PBS buffer. Cells were washed twice with 1× PBS, centrifuged at 500 g, at 4°C for 5 minutes, resuspended in 10 ml of 1× PBS and both steps were repeated.

Satb1 isoforms cloning

Murine thymocytes total RNA was used for reverse transcription. The cDNA was amplified utilizing primers specific for mouse *Satb1*: SATB1-fwd (5´-GCC AGA TCT ATG GAT CAT TTG AAC GAGGC-3´, with integrated restriction enzyme site for BglII and SATB1-rev (5´- GCC CTG CAG TCA GTC TTT CAA GTC GGCAT-3´, with an integrated restriction enzyme site for PstI. The PCR product was cloned in a TOPO TA vector (Thermo Fisher Scientific, pCR™ II-TOPO®) and 20 clones with *Satb1* inserts were analyzed upon restriction enzyme digestion and Sanger sequencing indicating the presence of *Satb1* cDNAs with different length. BLAST search indicated that the cloned cDNAs encoded a short SATB1 isoform of 764 amino acids (UniProtKB – Q60611) and a long SATB1 isoform of 795 amino acids (UniprotKB – E9PVB7).

Custom SATB1 antibodies production

The first 330 amino acids of SATB1 short isoform (UniProtKB - Q60611, 1-764aa) fused to a 6x histidine tag at the N-terminus were expressed in *E. coli* and the antigen was utilized for the immunization of New Zealand rabbits and the production of SATB1 anti-sera (Davids Biotechnology). Rabbit polyclonal immunoglobulin specific to SATB1 N-terminal 330 amino acids were purified with column chromatography with the immobilized antigen used for immunization. The long SATB1-specific antisera were produced by Davids Biotechnology upon immunization of New Zealand rabbits with the GKGESRGVFLPSLLTPAPWPHAA peptide (corresponding to the extra peptide identified in the long SATB1 isoform) and subsequent purification of rabbit polyclonal peptide-specific immunoglobulins using affinity purification.

SATB1 long isoform detection and antibody validation

Thymocyte protein extracts were prepared from 4-6 weeks old female C57BL/6 mice. Thymocytes were incubated at room temperature for 30 minutes with rotation, in 1 ml EBC lysis buffer with high salt concentration (500 mM NaCl, 50 mM Tris pH=7.5, 5% Glycerol, 1% Nonidet P-40, 1 mM $MgCl_2$, 1× Protease Inhibitors, 1 mM PMSF). 0.8-1 mg protein extract was incubated with 8 µg SATB1 long isoform antibody, overnight at 4°C, on an end-to-end-rotator. The immune-complexes were incubated with 20 µl protein A/G magnetic beads (Sigma Aldrich, 16-663) for 2 hours at 4°C on an end-to-end rotator. The flowthrough (SATB1 long isoform immunodepleted fraction) was kept and beads were washed 3 times with buffer I (300 mM NaCl, 50 mM Tris pH=7.5, 5% Glycerol, 0.05% Nonidet P-40, 1 mM PMSF), 2 times with Buffer II (400 mM NaCl, 50 mM Tris pH=7.5, 5% Glycerol, 1 mM PMSF) and boiled in SDS loading buffer for 10 minutes at 95°C. The flow-through was incubated with 8 µg SATB1 antibody recognizing epitopes on both isoforms, overnight at 4°C, on an end to end rotator. The immune-complexes were incubated with 20 µl protein A/G magnetic beads (Sigma Aldrich, 16-663) for 2 hours at 4°C on an end to end

rotator. The flowthrough (SATB1 both isoforms immunodepleted fraction) was kept and beads were washed 3 times with buffer I (300 mM NaCl, 50 mM Tris pH=7.5, 5% Glycerol, 0.05% Nonidet P-40, 1 mM PMSF), 2 times with Buffer II (400 mM NaCl, 50 mM Tris pH=7.5, 5% Glycerol, 1 mM PMSF) and boiled in SDS loading buffer for 10 minutes at 95°C. The immunoprecipitated proteins were resolved with SDS PAGE on an 8% gel. Proteins were transferred to a nitrocellulose membrane at 320 mA for 1.5 hours at 4°C. The membrane was blocked with 5% BSA at room temperature for 1 hour and then washed three times with TBST, 5 minutes each. The membrane was initially incubated with an antibody against the long SATB1 isoform (1:200 dilution; Davids Biotechnology, custom-made), and upon antibody stripping it was blotted again using an antibody against both isoforms of SATB1 (1:100 dilution; Santa Cruz Biotechnology, sc-376096).

Stranded-total-RNA sequencing

Freshly isolated thymocytes from female animals were resuspended in 1 ml of TRIzol Reagent (Invitrogen, 15596026) and RNA was isolated according to manufacturer's protocol. The aqueous phase with RNA was transferred into a tube and combined with 10 µg of Linear Acrylamide (Ambion, AM9520), 1/10 of sample volume of 3M CH3COONa (pH 5.2), 2.5 volumes of 100% Ethanol and tubes were mixed by flipping. Samples were incubated at –80°C for 40 minutes. Samples were brought to 0°C and centrifuged at 16,000 g, at 4°C for 30 minutes. The supernatant was removed and the pellet was washed twice with 75% ethanol. The air-dried pellets were resuspended in 40 µl RNase-free water and incubated at 55°C for 15 minutes to dissolve. To remove any residual DNA contamination, RNase-free DNase Buffer was added to samples until 1× final concentration together with 20 units of DNase I (NEB, M0303L) and incubated at 37°C for 20 minutes. Samples were then additionally purified using the RNeasy Mini Kit (Qiagen, 74104)

according to the manufacturer's protocol. The quality of RNA was evaluated using the Agilent 2100 Bioanalyzer with Agilent RNA 6000 Nano Kit (Agilent Technologies, 5067-1511). Libraries were prepared using the Illumina TruSeq Stranded Total RNA kit with ribosomal depletion by Ribo-Zero Gold solution from Illumina according to the manufacturer's protocol and sequenced on an Illumina HiSeq 4000 (2× 75 bp).

Raw reads were mapped to the mm10 mouse genome using HISAT2[63]. Only mapped, paired reads with a map quality >20 were retained. Transcripts were assembled with StringTie[64] using an evidence-based Ensembl-Havana annotation file. Transcripts and genes were summarized using featureCounts[65] and statistically evaluated for differential expression using DESeq2[66]. When application required an intra-sample transcript comparison, DESeq2 values were further normalized to the gene length.

The list of exons was extracted from the mouse GENCODE gene set (version M20) using a customized script. Overlapping exons were merged and final exon-exon and intron-exon lists were generated. The lists were converted to 2 bp junctions (1 bp covering the first exon and 1 bp covering the second exon or the intron sequence). Both lists were intersected and purified to retain only paired exon-exon and intron-exon junctions from the same genes, i.e. embedded or overlapping genes and other unconventional cases were filtered out. Coverage of the junctions was assessed using the bedtools multicov -q 10 -s -split command and utilizing the HISAT2 mapped bam files from the RNA-seq analysis. The resulting exon-exon and exon-intron files from both WT and *Satb1* cKO were combined, junctions were paired and the unpaired junctions were filtered out. Junctions were split into the 5-prime and 3-prime end of the exon. Splicing efficiency was estimated for entire genes after summing up the coverage of all junctions from the same gene. Genes with overall exon-exon WT coverage (all exon-exon junctions together for all biological

replicates) lower than 50 were filtered out. The splicing efficiency was determined as the intron/exon coverage ratio and its changes as a difference between *Satb1* cKO – WT intron/exon ratios. Moreover, the SATB1 binding sites' dataset (GSE173446[19]) was intersected with the junctions to search for a potential dependency of splicing on the SATB1 presence (Supplementary Fig. 2d). The SATB1 binding propensity was calculated as the sum of fold change enrichments of all SATB1 peaks (for each peak summit against random Poisson distribution with local lambda, based on MACS2)[67] overlapping each gene and normalized to 1 kbp.

Alternative splicing was analyzed using the Whippet program[68] with --biascorrect flag and using both options: with and without the --bam flag (using the HISAT2 mapped bam files from the RNA-seq analysis, ensuring coverage of unannotated splice-sites and exons). In both cases, the mouse GENCODE gene set (version M11) was used to build the index file. The results from the whippet-delta script were filtered for results with probability >=0.9 and absolute delta psi value >=0.1. Out of 150,382 and 130,380 events it yielded 3,281 (2,015 genes) and 1,717 (1,077 genes) events that passed the filtering step for the bam-file-supplemented and without the bam-file analyses, respectively. Moreover, the analysis of back-splicing (circular RNA) revealed 639 events (519 genes) being underrepresented and 443 events (374 genes) overrepresented in the *Satb1* cKO.

RT-qPCR

Isolated thymocytes were resuspended in 1 ml of TRIzol Reagent (Sigma Aldrich, T9424) and RNA was isolated according to the manufacturer's protocol. Isolated RNA (5 µg) was decontaminated by incubation with 4 units of DNase I (NEB, M0303L) at 37°C for 30 minutes. The reaction was stopped by adding 10 µl of DNase Inactivation Reagent (Ambion, 8174G) and incubating at 70°C for 10 minutes. The supernatant was transferred to a new tube and RNA was precipitated by adding 10 µg of Linear Acrylamide (Ambion, AM9520), 2.5X volumes of 100%

Ethanol and incubated at –80°C for 30 minutes. The supernatant was removed and the pellet was washed twice with 75% Ethanol. The air-dried pellets were resuspended in RNase-free water and incubated at 55°C for 15 minutes to dissolve. For reverse transcription, 1 µg of RNA was combined with 1 µl of oligo dTs (100 pmol/µl), 1 µl dNTPs (10 mM) and topped up with ddH_2O to 13 µl. Samples were denatured at 65°C for 5 minutes and transferred on ice. Samples were combined with 4 µl 5X Minotech RT assay buffer, 1 µl 0.1 M DTT, 1 µl RNase inhibitor (40 U/µl) and 1 µl Minotech RT enzyme (Minotech, 801-1). The mixture was incubated at 45°C for 60 minutes and then heat-inactivated at 70°C for 15 minutes. The original transcripts were quantified with qPCR, using SYBR Select Master Mix (Applied Biosystems, 4472908) according to the manufacturer's instructions with the following primers: long *Satb1* isoform (fwd: TTCTTACCAAGCCTGCTGACC, rev: TGGTCTTCTGCCGGTTTTCC), all short *Satb1* isoforms (fwd: CAGAACAGATTCAGCAGCAG, rev: TGGTCTTCTGCCGGTTTTCC) and *Dnmt1* (fwd: GCAGCCTATGAAGATTGAAGAG, rev: CCTGGCTAGATAGAGTGGTTTG).

SATB1 co-immunoprecipitation coupled to mass spectrometry

Thymocyte protein extracts were prepared from eight male 4-6 weeks old C57BL/6 mice. Thymocytes were incubated at room temperature for 30 minutes with rotation, in 1 ml lysis buffer (150 mM NaCl, 50 mM Tris pH=7.5, 5% Glycerol, 1% Nonidet P-40, 1 mM $MgCl_2$, 200 U benzonase, 1× Protease Inhibitors, 1 mM PMSF). 24 mg of protein extract were precleared using 100 µl of Dynabeads® Protein G (Life Technologies, 10004D) at 4°C for 1.5 hours on an end-to-end rotator. 50 µl of beads pre-blocked with 15 µg rabbit anti-SATB1 or rabbit IgG sera (Santa Cruz Biotechnology, C2712) at 4°C for 4 hours rotating and crosslinked at room temperature for 30 minutes with tilting/rotation using cross-linker Bis(sulfosuccinimidyl) suberate BS3 (Thermo Fisher Scientific, 21580). Precleared lysates were subjected to immunoprecipitation by incubation

with Dynabeads crosslinked with anti-SATB1 or IgG at 4°C for 30 minutes. Beads were washed three times with buffer I (150 mM NaCl, 50 mM Tris pH=7.5, 5% Glycerol, 0.05% Nonidet P-40, 1mM PMSF), twice with Nonidet P-40 free Buffer II (150 mM NaCl, 50 mM Tris pH=7.5, 5% Glycerol, 1 mM PMSF) and boiled at 95°C for 5 minutes.

Proteins co-Immunoprecipitated with SATB1 were resolved via SDS-PAGE in a 10% polyacrylamide gel. The gel was stained with silver nitrate compatible with mass spectrometry fixation: 50% MeOH, 12% acetic acid, 0.05% Formalin for 2 hours and washed with 35% ethanol for 20 minutes for 3 times. Sensitization followed with 0.02% $Na_2S_2O_3$ for 2 minutes and washes performed with H_2O for 5 minutes 3 times. Staining was performed with 0.2% $AgNO_3$, 0.076% formalin for 20 minutes and washes were with H_2O for 1 minute 2 times. Development took place with 6% Na_2CO_3, 0.05% formalin, 0.0004% $Na_2S_2O_3$. Staining was stopped with 50% MeOH, 12% acetic acid for 5 minutes.

Ten pairs of protein bands (anti-SATB1, IgG) were excised from silver-stained polyacrylamide gels and cut into small pieces. Gel pieces were covered with destain solution (30 mM potassium ferricyanide, 100 mM sodium thiosulfate) and vortexed for 10 minutes in order to remove silver nitrate. For the reduction and alkylation of the cysteine residues, the gel pieces were covered with 100 µl 10 mM DTT and shaked for 45 minutes at 56°C followed by 45 minutes shaking at room temperature with 100 µl 55 mM iodoacetamide. Proteins were digested in 30 µl of diluted Trypsin solution and incubated overnight at 37°C. The next day, the supernatant was collected. For the extraction from the gel matrix of generated peptides, gel pieces were shaken for 20 minutes first in 50 µl 50% acetonitril (ACN) and finally in 50 µl 0.1% TFA/50% ACN. Peptide solutions were centrifuged by Speed Vac until dry powder remained and then analyzed by means

of liquid chromatography combined with mass spectrometry analysis (nanoLC-MS/MS), as previously described[69].

Peptide intensities of each experiment were normalized based on the mean difference of their distribution (log2 intensity) with the reference sample (SATB1 IP-MS 2nd biological replicate). Missing values were imputed using the mean values of each peptide within a given study group (SATB1 IP-MS or the control – IgG IP-MS), plus random noise equal to the mean observed variability in the dataset. Dataset variability was calculated as the standard deviation of the difference between all the biological replicates of a given group and the group mean. Protein abundance was calculated using the sum of peptide intensities. Differentially abundant proteins were selected after comparing the t-test p-value (using log2 intensities) and the fold change for each protein. P-values were adjusted for multiple hypothesis testing error using the Benjamini-Hochberg method. Threshold for selection of differentially abundant proteins was an adjusted p-value < 0.05 and a fold change $> 2\times$. Proteins that were uniquely identified in the SATB1 IP-MS dataset and proteins commonly identified with a significantly higher abundance in the SATB1 IP-MS replicates were considered for the downstream analysis as enriched proteins.

Protein-protein interaction data were downloaded from the STRING database[70]. STRING database mappings from Ensemble protein IDs to Uniprot IDs were used to map the interaction data with the experimental results. Protein-protein interaction network was build using the NetworkX Python library[71]. To cluster network nodes, vector representations were initially extracted for each node, using the node2vec algorithm[72] and followed by k-means clustering. GO and pathway enrichment analysis were performed using g:Profiler tool[73] using the default settings.

Identification of SATB1 phosphosite S635

DNA affinity chromatography coupled with mass spectrometry was performed as previously described[74,75] to identify associated proteins. A region of 151 bp, part of the RHS6 DNase I hypersensitive site of the TH2-LCR[76,77] was cloned into TOPO-TA vector using following primers: RP1-fwd CTTCCATTTGCTGGCCTCT; RP2-rev CCTGCATCTGATACTTAGACGTA. Two types of biotinylated oligonucleotides were utilized. Targeted fragment was biotinylated by PCR amplification with the following primers: biotinT7-fwd Biotin-d(CTCGAGTAATACGACTCACTATAGG); M13-rev AACAGCTATGACCATG. The same primers were used to prepare oligonucleotide for the negative selection (preclearing), by amplification from the TOPO-TA vector without the RHS6 region. 1 mg of M-280 Streptavidin Dynabeads (Invitrogen, 11205D) were resuspended and washed three times according to the manufacturer's instructions. 100 µl of 2× Binding & Wash buffer (10 mM Tris pH=7.5, 1 mM EDTA, 2 M NaCl) containing 10 µg of the biotinylated oligonucleotide in an equal volume of water was added. The beads with the oligonucleotide were incubated for 15 minutes with rotation at room temperature. Beads were collected on a magnet and further washed with 1× Binding & Wash buffer and once with DNA binding buffer (20 mM HEPES pH=7.9, 0.1 mM KCl, 0.2 mM EDTA, 0.01% NP-40, 0.5 mM DTT, 0.2 mM PMSF, 10% Glycerol) supplemented with 0.1 mg/ml oligo dI:dC and poly dI:dC. Thymocyte nuclear extracts (5 mg) were first negatively selected by the "preclearing" biotinylated oligonucleotide and then positively selected utilizing the biotinylated RHS6 sequence. The biotinylated oligonucleotides used for the positive selection of bound thymocyte proteins were boiled and electrophoresed on a denaturing polyacrylamide gel. Upon Coomassie blue silver staining, individual slices of the positively selected samples, the negatively selected samples and washes were utilized in parallel for nanoLC-MS/MS analysis as

previously described[69]. Subsequent protein identification was done using Mascot and Sequest software.

Immunofluorescence confocal and super-resolution microscopy experiments

Freshly isolated thymocytes were incubated for 60 minutes (producing the best results compared to 30 and 240 minutes) at 37°C in complete DMEM (GIBCO, 11995-073) medium with 10% serum with 2 mM 5-Fluorouridine (FU; Sigma Aldrich, F5130) or directly attached on poly-D-lysine-coated coverslips. For super-resolution microscopy, high precision Zeiss squared coverslips of 1.5H thickness (0.170+-0.005 mm; Marienfeld Superior, 0107032) were treated with 1 M HCl overnight, rinsed with ddH_2O and then stored in absolute ethanol. Right before the experiment, coverslips were coated by dipping in 0.1 mg/ml poly-D-lysine solution (Sigma Aldrich, P6407). Attached cells were washed once with 1× PBS. Coverslips to be treated with 1,6-hexanediol (Sigma Aldrich, 804308) were incubated for 5 minutes at room temperature with the 1,6-hexanediol solution, carefully washed twice with 1× PBS and then fixed for 10 minutes on ice with 4% formaldehyde (Pierce, 28908) in 1× PBS. Fixed cells were permeabilized with 0.5% Triton-X in 1× PBS for 5 minutes on ice. Cells were washed three times with 1× PBS for 5 minutes each and blocked for 30 minutes at room temperature with Blocking Buffer [0.4% acetylated BSA (Ambion, AM2614) in 4× SSC] in a humidified chamber. Cells were incubated for 1.5 hours at room temperature with primary antibodies (see the table below) in Detection Buffer (0.1% acetylated BSA, 4× SSC, 0.1% Tween 20) in a humidified chamber. The excess of primary antibodies was washed away by three washes, for 5 minutes each, with Wash Buffer (4× SSC, 0.1% Tween 20). Cells were incubated for 60 minutes at room temperature with the secondary antibodies in Detection Buffer (0.1% acetylated BSA, 4× SSC, 0.1% Tween 20) in a humidified chamber. The excess was washed away by three washes, for 5 minutes each, with Wash Buffer (4× SSC, 0.1%

Tween 20). The coverslips for 3D-SIM experiments were stained for 5 minutes at room temperature with DAPI in 1× PBS (0.85 μg/ml) and then washed three times in 1× PBS. The coverslips for STED experiments were directly mounted with 90% glycerol + 5% (w/v) n-propyl gallate non-hardening medium and sealed with a transparent nail polish.

Summary of antibodies used in super-resolution microscopy experiments:

	Primary antibody			Secondary antibody **STED**			Secondary antibody **3D-SIM**		
Factor	**Vendor**	**Cat. No.**	**Dil.**	**Name**	**Species specificity**	**Dil.**	**Name**	**Species specificity**	**Dil.**
long SATB1 isoform	Davids Biotechnology	n/a	1:500	Abberior Star Red or Alexa Fluor 555	goat anti-rabbit	1:100 or 1:500	Alexa Fluor 488	goat anti-rabbit or donkey anti-rabbit	1:500
all SATB1 isoforms	Davids Biotechnology	n/a	1:500	Abberior Star Red	goat anti-rabbit	1:100	Alexa Fluor 488	goat anti-rabbit	1:500
all SATB1 isoforms	Santa Cruz Biotechnology	sc-5990	1:200	–	–	–	Alexa Fluor 488	donkey anti-goat	1:500
5-fluorouridine	Sigma Aldrich	B2531	1:250	Abberior Star 580	goat anti-mouse	1:100	Alexa Fluor 568	goat anti-mouse	1:500

The STED experiment images were acquired using an inverted microscope DMi8 with laser scanning confocal head Leica TCS SP8, equipped with STED 3X module, 100x/1.4 oil immersion objective and 660 nm continual and 775 pulse depletion lasers. Depletion lasers were set to 60% and typically only a single representative z-stack from the center of each cell was scanned to reduce the effect of photobleaching and to maximize the lateral resolution, with line accumulation set to 8 and speed of 400 Hz. Raw images were deconvoluted using the Huygens Professional imaging software. The final images were analyzed using custom-made macros in Fiji software[78]. Cells from the representative middle z-stack were manually selected for the analysis and the integrated density was calculated by the measure tool of Fiji. The pixel-based colocalization analysis of selected cells was performed using the Coloc2 plugin. SATB1 scans rotated by 90° served as a negative control for the colocalization with FU. The presented images have artificially increased contrast and brightness for better visualization.

The 3D-SIM experiment images were acquired using the DeltaVision OMX V4 imaging platform equipped with PlanApo N 60x/1.42 oil immersion objective, pco.edge 5.5 sCMOS cameras and 405, 445, 488, 514, 568 and 642 nm lasers. Spherical aberration was minimized using immersion oil with RI 1.516 for sample acquisition. Images were acquired over the majority of the cell volume in z-dimension with 15 raw images per plane (five phases, three angles), providing ~115-135 nm lateral and ~340-350 nm axial resolution for 488/568 nm lasers, respectively. Image reconstruction and deconvolution was performed by the SoftWoRx software using channel-specific OTFs with Wiener filter set to 0.01 for DAPI and 0.001 for the other channels. For data analysis, mostly a single representative z-stack from the center of the cell was manually selected to minimize any effect of artefacts. The final images were analyzed using custom-made macros in Fiji software[78]. Cells were manually selected for the analysis and then the exact nuclear borders were drawn based on the DAPI signal. This was used to calculate the integrated density by the measure tool of Fiji as well as to perform the pixel-based colocalization analysis using the Coloc2 plugin. SATB1 scans rotated by 90° served as a negative control for the colocalization with FU. The DAPI zonation was achieved using the IsoData Classifier in combination with the machine learning Trainable Weka Segmentation plugin. The selection of the resulting zones was overlaid with SATB1 speckles, identified as points using Find Maxima function in Fiji with prominence set to 2000 or 5000 depending on the biological replicate. For each cell, the number of points in each zone was converted to its relative proportion in respect to the total number of speckles in the cell. The presented images have artificially increased contrast and brightness for better visualization.

For the colocalization immunofluorescence experiments analyzed with confocal microscopy (Supplementary Fig. 1b) we utilized a commercially available antibody against SATB1 detecting both short and long isoforms (1:100; Santa Cruz Biotechnology, sc-376096) and

our custom-made polyclonal antibody (1:500; Davids Biotechnology) raised against the extra SATB1 peptide of the long isoform, following the protocol described earlier. Coverslips were mounted with hardening medium ProLong Gold with DAPI (Invitrogen, P36935). Images were taken using the inverted microscope DMI6000 CS with laser scanning confocal head Leica TCS SP8, equipped with 63x/1.40 oil immersion objective.

Nuclear matrix preparation

Freshly isolated thymocytes were attached to poly-D-lysine coated coverslips. Soluble proteins were removed by extraction in cytoskeletal buffer (CSK: 10 mM Pipes pH 6.8, 300 mM sucrose, 100 mM NaCl, 3 mM $MgCl_2$, 1 mM EGTA, 2 mM VRC) supplemented with 0.5% Triton X-100 for 3.5 minutes at 4°C. The first group of cells was cross-linked with 4% PFA in 1× PBS for 10 minutes at 4°C, followed by three washes in 70% Ethanol. The other groups were subjected to DNase treatment in 300 µl DNase Buffer (10 mM Tris-HCl pH 7.5, 2.5 mM $MgCl_2$, 0.5 mM $CaCl_2$) combined with DNase I (10 U = 5 µl; NEB, M0303L) at 37°C for 40 minutes. The last group was subjected to RNase A treatment (10 µl = 100 µg; Qiagen, 1007885) in PBS at 37°C for 40 minutes. After the enzymatic treatment, nucleic acid fragments were extracted by a 5-minute treatment on ice with CSKpremix (without Triton X-100) supplemented with 250 mM Ammonium Sulfate, followed by one 1× PBS wash and then they were fixed as previously described. Alternatively, they were further extracted with CSKpremix with 2M NaCl, followed by one 1× PBS wash and then fixed. After fixation, cells were washed twice with 1× PBS. Samples were blocked for 30 minutes with Blocking Buffer as previously described and stained with an anti-SATB1 antibody targeting all isoforms (Santa Cruz Biotechnology, sc-5990) and a donkey anti-goat Alexa Fluor 546 secondary antibody. Coverslips were mounted with hardening medium ProLong Gold with DAPI (Invitrogen, P36935). Images were taken using the inverted microscope DMI6000 CS with

laser scanning confocal head Leica TCS SP8, equipped with 63x/1.40 oil immersion objective. Images were scanned at 600 Hz speed, unidirectionally with frame average set to 3. In the experiment with double DNase I + RNase A treatment, no cells were detectable using fluorescence microscopy, hence the remaining cellular shells were identified in bright field. The final images were analyzed using the Fiji software[78]. The presented images have artificially increased contrast and brightness for better visualization.

Raman spectroscopy

Isolated thymocytes were washed once with 1× PBS and then incubated in 10% 1,6-hexanediol (Sigma Aldrich, 240117) in 1× PBS solution (Sigma Aldrich, P4417) for 10 minutes at room temperature, side by side with a non-treated control. Samples were fixed with 1% formaldehyde (final conc.; Pierce, 28908) for 10 minutes and then quenched with glycine to a 0.125 M final concentration and incubated at room temperature for 5 minutes, while rocking. Cells were washed five times with 1× PBS. For measurements, a drop of cells was loaded on a stainless-steel microscopic slide (Renishaw, UK) and imaged through an Olympus 60x water immersion objective lens with a numerical aperture (NA) of 1.2 and a working distance of 280 μm (UPLSAPO60XW/1.2, Olympus, Tokyo, Japan). Raman measurements were made by a modified Raman Spectrometer (LabRAM HR, HORIBA Scientific, Lille, France). The excitation laser line used had a central wavelength at 532 nm and the resulting laser power on the sample was ~10 mW. The laser spot spatial diameter was approximately 0.6 μm, with an axial length of about 0.5 μm. A grating of 600 groves was used that resulted in a Raman spectral resolution of around 2 cm^{-1}. A temperature-controlled stage (PE120-XY, Linkam) was coupled with the microscope stage that kept cells temperature constant. Spectral calibration was performed with a SiO_2 reference sample, presenting a single peak at 520.7 cm^{-1}. Raman signal was acquired in the spectral range between

300 and 3,150 cm^{-1}. Acquisition time was set to 10 seconds with a spectral accumulation of 3 spectra/point. All Raman spectra acquired followed this processing methodology: a) cosmic rays were removed by an internal function (Despike, LabSpec LS6, Horriba); b) background signal was subtracted from the raw Raman spectral data using a polynomial function; c) all spectra were normalized in intensity by an internal function (Unit Vector, LabSpec LS6, Horriba). PCA was performed using the Raman PCA Tool[79], publicly available through (https://sourceforge.net/projects/ramantoolset/).

Construction of CRY2-mCherry SATB1 recombinant proteins

For all CRY2 constructs, the pCMV-CRY2-mCherry vector was used (a gift from Won_Do Heo; Addgene plasmid # 58368). As a positive control, the N-terminal part of FUS protein was used from the plasmid pHR-FUS_N-mChr-CRY2WT (a gift from Clifford Brangwynne; Addgene plasmid # 101223). The N-terminal part of SATB1 was cloned into the pCMV-CRY2-mCherry vector using a single BspEI restriction enzyme site from the full-length construct. The IDR part of all *Satb1* isoforms (incl. the S635A mutated version) and also the N-terminal part of *FUS* was PCR amplified from plasmids, generating new restriction enzyme sites for XhoI and BamHI, using the following primers: for *Satb1* fwd: GTCTACTCGAGCACGAAAGGAAGAGGACCCC, rev: GATTGGATCCTTACACGGAAATTTTGGTTCGTG, for *FUS* fwd: GTCTACTCGAGCAATGGCCTCAAACGATTATACC, rev: GATTGGATCCTTATCCACGGTCCTGCTGTCCATAG. The sequence encoding the SV40 NLS signal peptide PKKKRKV was isolated from a lab's plasmid using BspEI and SalI enzymes and inserted into CRY2-mCherry-IDR-SATB1 constructs between BspEI and XhoI sites, embedding it between mCherry and the IDR part of SATB1. Bacteria were grown in Luria-Bertani Broth at 37°C and plasmid DNA was isolated using the Nucleobond Xtra midi kit (MACHEREY-NAGEL,

740410), according to the manufacturer's instructions. PCR reactions were performed utilizing the Phusion High-Fidelity PCR Master Mix (NEB, M0531L) to prevent any mutations. For all restriction reactions the respective NEB reagents were used according to the manufacturer's instructions. Ligation reactions were performed using T4 DNA Ligase (Minotech, 202-2) according to the manufacturer's instructions. Ligation products were transformed into DH5a competent cells via 42°C heat shock for 45 seconds. All constructs were sequence-verified using Sanger sequencing in Macrogen Europe.

Tissue cultures and transient transfection

Cells were cultured in the complete growth medium DMEM (Gibco, 11995-073) supplemented with 10% Fetal Bovine Serum (Sigma Aldrich, F4135) and with 2 mM L-glutamine (Gibco, 25030) in a 5% CO_2 incubator at 37°C, until 70% confluency. Before the experiment, cells were washed in Dulbecco's PBS (DPBS; Gibco, 14200067) without Mg^{2+} and Ca^{2+}. Cells were treated for 3-5 minutes at 37°C in 1× trypsin solution until detached. Trypsin was quenched by complete growth medium and cells collected. For optoDroplet experiments, 800 ng of plasmid DNA was combined with 50 µl of Opti-MEM I Reduced Serum Medium and pipetted onto a glass bottom dish (MatTek, P35GC-0-14-C). Next, 2 µg of Lipofectamine 2000 (Invitrogen, 11668-027) was carefully mixed with 50 µl Opti-MEM I Reduced Serum Medium and it was incubated for 5 minutes at room temperature. Lipofectamine/OptiMEM mix was slowly and drop-wise added to the DNA/OptiMEM mixture on the glass bottom dish and incubated for 30 minutes at room temperature. 50,000 of NIH/3T3 ATCC CRL-1658 cells were added to the DNA/Lipofectamine/OptiMEM mixture and they were incubated at 37°C in a humidified 5% CO_2 incubator for 6 hours. After six hours, 2 ml of the growth medium with antibiotics

(penicillin/streptomycin to the final concentration 100 I.U./ml / 100 μg/ml) was added and continued transfection until ready to assay (24-48 h post transfection).

Live cell microscopy

Live cell imaging was performed in a live imaging box at 37°C with 5% CO_2, using the inverted microscope DMI6000 CS with laser scanning confocal head Leica TCS SP8, equipped with a 63x/1.40 oil immersion objective. To ensure the minimal pre-activation effect, cells were located with dim bright field illumination. In all cases presented, only a single plane in the center of the cell was scanned. CRY2 activation was achieved by 488 nm Argon laser illumination every two seconds, complemented with DPSS 561 nm laser illumination for mCherry detection. During the inactivation period, only the 561 nm laser was used to detect the mCherry signal. The scanning parameters were: PinholeAiry 1.5 AU, frame average 2 and speed to 600 Hz, scanned unidirectionally. Images were analyzed using custom-made macros in Fiji software[78] and data were processed in Bash and R. Briefly, images were corrected for movement using the StackReg plugin[80]. After basic pre-processing, droplets were identified in each cell for each time point using the Analyze Particles function of Fiji. The area of droplets was used to determine the droplet size. The number of droplets was normalized to the size of a cell. The images presented have artificially increased contrast and brightness for better visualization. For the FRAP experiments, the scanning speed was set to 1,000 Hz, bidirectionally (0.54 s / scan) and every time a selected point was photobleached for 300 ms. Bleach point mean values were background subtracted and corrected for fluorescence loss using the intensity values from the entire cell. The data were then normalized to mean pre-bleach intensity and fitted with exponential recovery curve in Fiji or in frapplot package in R.

Structure of SATB1 and the use of predictors

SATB1 domains used in Fig. 1a were previously described[20]. The prediction of IDR regions in Fig. 4a is based on PONDR VL3 score (http://www.pondr.com/) and it is shown only for the long SATB1 isoform. Similarly, the sequence of the long SATB1 isoform was analyzed using the hidden-Markov model algorithm PLAAC to predict prion-like domains[81], using background frequencies from *S. cerevisae*. For better lucidity, the background probabilities are not shown.

Breast cancer data processing

Breast invasive carcinoma cohort data (BRCA) from the TCGA were obtained from the FireBrowse repository of the Broad Institute of MIT & Harvard (http://firebrowse.org). For the correlation experiment between chromatin accessibility and RNA expression, the ATAC-seq bigwig files were downloaded[51] and signal from a region encompassing the extra exon of the long *SATB1* isoform (chr3:18351000-18351700) was extracted using multiBigwigSummary from the deeptools package[82]. The signal was correlated with summarized values of the two short isoforms (uc003cbh.2 and uc003cbj.2) and separately with the long isoform (uc003cbi.2) RNA-seq values (level 3, isoform-specific normalized RSEM dataset, version 2016_01_28). Patient TCGA-A2-A0ET-01A was removed as an outlier. The same RNA-seq values were also used for correlation with the metadata on the pathological T stage of cancer patients. Next, we analyzed the recurrent copy number alterations using the R package GAIA[83], using the SNP6 level 3 segmented sCNA minus germline CNV dataset. The output file with tumor samples was further processed by the GenomicRanges package[84] and annotated by the findOverlaps function. Survival plots were constructed using the survival package in R[85], utilizing the normalized RNA-seq data and clinical metadata from TCGA. RNA-seq data were transformed into z-scores as follows: z = [(value gene X in tumor Y) – (mean gene X in all tumors with CNV segment mean value <|0.2|)] / (standard

deviation X in all tumors with CNV segment mean value <|0.2|). Patients were divided into groups with low and high estrogen receptor levels. Moreover, patients were divided based on the relative expression levels of each tested isoform into UPregulated, DOWNregulated and unchanged groups, using the z-score threshold 1.65 (~ $P = 0.0495$). Survival plots for individual *SATB1* isoforms were plotted. Short isoform uc003cbh.2 and long isoform uc003cbi.2 were used for visualization. Different z-score thresholds were also tested. We reasoned that normalization to the normal tissue samples would bias the results due to possible infiltration of T cells (predominantly expressing *SATB1*).

Acknowledgements

We would like to thank Despina Tsoukatou, Manouela Kapsetaki, George Papadogkonas and Joseph Papamatheakis for fruitful discussions and assistance in the lab. This work was supported by the European Union (European Social Fund ESF) and Greek national funds through the Operational Program 'Education and Lifelong Learning' of the National Strategic Reference Framework (NSRF) Research Funding Program ARISTEIA [MIRACLE 42], by FONDATION SANTE (X-COAT) and by Chromatin3D-H2020-MSCA-ITN (GA642934). Author V.M.P acknowledges the support of Stavros Niarchos Foundation within the framework of the project ARCHERS ("Advancing Young Researchers' Human Capital in Cutting Edge Technologies in the field of Systems Biology Approaches and Personal Genomics for Health and Disease Treatment"). We acknowledge the Light Microscopy Core Facility, IMG CAS, Prague, Czech Republic, supported by MEYS (LM2018129, CZ.02.1.01/0.0/0.0/18_046/0016045) and RVO: 68378050-KAV-NPUI, for their support with the super-resolution imaging and image analysis presented herein. We thank the personnel of the Proteomics Facility at the Institute of Molecular Biology and Biotechnology, M. Aivaliotis and N. Kountourakis, for the Mass spectrometry analysis of tryptic

peptides by nanoflow liquid chromatography with tandem mass spectrometry. Moreover, the results shown here are in part based upon data generated by the TCGA Research Network: https://www.cancer.gov/tcga. The funders had no role in study design, data collection and analysis, decision to publish, or preparation of the manuscript.

References

1. Alberti, S., Gladfelter, A. & Mittag, T. Considerations and challenges in studying liquid-liquid phase separation and biomolecular condensates. *Cell* **176**, 419–434 (2019).
2. Banani, S. F., Lee, H. O., Hyman, A. A. & Rosen, M. K. Biomolecular condensates: organizers of cellular biochemistry. *Nat. Rev. Mol. Cell Biol.* **18**, 285–298 (2017).
3. Shin, Y. & Brangwynne, C. P. Liquid phase condensation in cell physiology and disease. *Science* **357**, eaaf4382 (2017).
4. Gotor, N. L. *et al.* RNA-binding and prion domains: the Yin and Yang of phase separation. *Nucleic Acids Res.* **48**, 9491–9504 (2020).
5. Wang, J. *et al.* A molecular grammar governing the driving forces for phase separation of prion-like RNA binding proteins. *Cell* **174**, 688-699.e16 (2018).
6. Pearce, M. M. P. & Kopito, R. R. Prion-like characteristics of polyglutamine-containing proteins. *Cold Spring Harb. Perspect. Med.* **8**, a024257 (2018).
7. Langdon, E. M. *et al.* mRNA structure determines specificity of a polyQ-driven phase separation. *Science* **360**, 922–927 (2018).
8. Peskett, T. R. *et al.* A liquid to solid phase transition underlying pathological huntingtin exon1 aggregation. *Mol. Cell* **70**, 588-601.e6 (2018).
9. Zhang, H. *et al.* RNA controls polyQ protein phase transitions. *Mol. Cell* **60**, 220–230 (2015).
10. Zhang, S., Hinde, E., Parkyn Schneider, M., Jans, D. A. & Bogoyevitch, M. A. Nuclear bodies formed by polyQ-ataxin-1 protein are liquid RNA/protein droplets with tunable dynamics. *Sci. Rep.* **10**, 1–18 (2020).

11. Williams, A. J. & Paulson, H. L. Polyglutamine neurodegeneration: protein misfolding revisited. *Trends Neurosci.* **31**, 521–528 (2008).

12. Franzmann, T. M. & Alberti, S. Prion-like low-complexity sequences: Key regulators of protein solubility and phase behavior. *J. Biol. Chem.* **294**, 7128–7136 (2019).

13. Bratek-Skicki, A., Pancsa, R., Meszaros, B., Lindt, J. V. & Tompa, P. A guide to regulation of the formation of biomolecular condensates. *FEBS J.* **287**, 1924–1935 (2020).

14. Baralle, F. E. & Giudice, J. Alternative splicing as a regulator of development and tissue identity. *Nat. Rev. Mol. Cell Biol.* **18**, 437–451 (2017).

15. Han, X. *et al.* Roles of the BRD4 short isoform in phase separation and active gene transcription. *Nat. Struct. Mol. Biol.* **27**, 333–341 (2020).

16. Ambadipudi, S., Biernat, J., Riedel, D., Mandelkow, E. & Zweckstetter, M. Liquid–liquid phase separation of the microtubule-binding repeats of the Alzheimer-related protein Tau. *Nat. Commun.* **8**, 275 (2017).

17. Boyko, S., Surewicz, K. & Surewicz, W. K. Regulatory mechanisms of tau protein fibrillation under the conditions of liquid–liquid phase separation. *Proc. Natl. Acad. Sci.* **117**, 31882–31890 (2020).

18. Batlle, C. *et al.* hnRNPDL phase separation is regulated by alternative splicing and disease-causing mutations accelerate its aggregation. *Cell Rep.* **30**, 1117-1128.e5 (2020).

19. Zelenka, T. *et al.* The 3D enhancer network of the developing T cell genome is controlled by SATB1. *bioRxiv* 2021.07.09.451769 (2021) doi:10.1101/2021.07.09.451769.

20. Zelenka, T. & Spilianakis, C. SATB1-mediated chromatin landscape in T cells. *Nucleus* **11**, 117–131 (2020).

21. Froemberg, A., Engeland, K. & Aigner, A. The Special AT-rich Sequence Binding Protein 1 (SATB1) and its role in solid tumors. *Cancer Lett.* **417**, 96–111 (2018).

22. Naik, R. & Galande, S. SATB family chromatin organizers as master regulators of tumor progression. *Oncogene* **38**, 1989–2004 (2019).

23. Sunkara, K. P., Gupta, G., Hansbro, P. M., Dua, K. & Bebawy, M. Functional relevance of SATB1 in immune regulation and tumorigenesis. *Biomed. Pharmacother.* **104**, 87–93 (2018).

24. Cai, S., Lee, C. C. & Kohwi-Shigematsu, T. SATB1 packages densely looped, transcriptionally active chromatin for coordinated expression of cytokine genes. *Nat. Genet.* **38**, 1278–1288 (2006).

25. Yasui, D., Miyano, M., Cai, S. T., Varga-WEisz, P. & Kohwi-Shigematsu, T. SATB1 targets chromatin remodelling to regulate genes over long distances. *Nature* **419**, 641–645 (2002).

26. Cai, S., Han, H.-J. & Kohwi-Shigematsu, T. Tissue-specific nuclear architecture and gene expession regulated by SATB1. *Nat. Genet.* **34**, 42–51 (2003).

27. Ghosh, R. P. *et al.* Satb1 integrates DNA binding site geometry and torsional stress to differentially target nucleosome-dense regions. *Nat. Commun.* **10**, 3221 (2019).

28. Galande, S., Dickinson, L. A., Mian, I. S., Sikorska, M. & Kohwi-Shigematsu, T. SATB1 cleavage by caspase 6 disrupts PDZ domain-mediated dimerization, causing detachment from chromatin early in T-cell apoptosis. *Mol. Cell. Biol.* **21**, 5591–5604 (2001).

29. Wang, Z. *et al.* The structural basis for the oligomerization of the N-terminal domain of SATB1. *Nucleic Acids Res.* **40**, 4193–4202 (2012).

30. Wang, Z. *et al.* Crystal structure of the ubiquitin-like domain-CUT repeat-like tandem of special AT-rich sequence binding protein 1 (SATB1) reveals a coordinating DNA-binding mechanism. *J. Biol. Chem.* **289**, 27376–27385 (2014).

31. Notani, D. *et al.* N-terminal PDZ-like domain of chromatin organizer SATB1 contributes towards its function as transcription regulator. *J. Biosci.* **36**, 461–469 (2011).

32. Cho, W.-K. *et al.* Mediator and RNA polymerase II clusters associate in transcription-dependent condensates. *Science* **361**, 412–415 (2018).

33. Sabari, B. R. *et al.* Coactivator condensation at super-enhancers links phase separation and gene control. *Science* **361**, eaar3958 (2018).

34. Kroschwald, S., Maharana, S. & Simon, A. Hexanediol: a chemical probe to investigate the material properties of membrane-less compartments. *Matters* **3**, e201702000010 (2017).

35. Kobayashi-Kirschvink, K. J. *et al.* Linear regression links transcriptomic data and cellular Raman spectra. *Cell Syst.* **7**, 104-117.e4 (2018).

36. Shin, Y. *et al.* Spatiotemporal control of intracellular phase transitions using light-activated optoDroplets. *Cell* **168**, 159-171.e14 (2017).

37. Bolognesi, B. *et al.* A concentration-dependent liquid phase separation can cause toxicity upon increased protein expression. *Cell Rep.* **16**, 222–231 (2016).

38. Maharana, S. *et al.* RNA buffers the phase separation behavior of prion-like RNA binding proteins. *Science* **360**, 918–921 (2018).

39. Dickinson, L. A., Joh, T., Kohwi, Y. & Kohwi-Shigematsu, T. A tissue-specific MAR/SAR DNA-binding protein with unusual binding site recognition. *Cell* **70**, 631–645 (1992).

40. Agostini, F., Cirillo, D., Bolognesi, B. & Tartaglia, G. G. X-inactivation: quantitative predictions of protein interactions in the Xist network. *Nucleic Acids Res.* **41**, e31 (2013).

41. Ding, X. *et al.* Amyloid-forming segment induces aggregation of FUS-LC domain from phase separation modulated by site-specific phosphorylation. *J. Mol. Biol.* **432**, 467–483 (2020).

42. Monahan, Z. *et al.* Phosphorylation of the FUS low-complexity domain disrupts phase separation, aggregation, and toxicity. *EMBO J.* **36**, 2951–2967 (2017).

43. Rai, A. K., Chen, J.-X., Selbach, M. & Pelkmans, L. Kinase-controlled phase transition of membraneless organelles in mitosis. *Nature* **559**, 211–216 (2018).

44. Shattuck, J. E., Paul, K. R., Cascarina, S. M. & Ross, E. D. The prion-like protein kinase Sky1 is required for efficient stress granule disassembly. *Nat. Commun.* **10**, 3614 (2019).

45. Wippich, F. *et al.* Dual specificity kinase DYRK3 couples stress granule condensation/dissolution to mTORC1 signaling. *Cell* **152**, 791–805 (2013).

46. Khare, S. P. *et al.* NF-κB signaling and IL-4 signaling regulate SATB1 expression via alternative promoter usage during Th2 differentiation. *Front. Immunol.* **10**, (2019).

47. Patta, I. *et al.* Dynamic regulation of chromatin organizer SATB1 via TCR-induced alternative promoter switch during T-cell development. *Nucleic Acids Res.* **48**, 5873–5890 (2020).

48. Schor, I. E., Rascovan, N., Pelisch, F., Alló, M. & Kornblihtt, A. R. Neuronal cell depolarization induces intragenic chromatin modifications affecting NCAM alternative splicing. *Proc. Natl. Acad. Sci.* **106**, 4325–4330 (2009).

49. Zhou, H.-L. *et al.* Hu proteins regulate alternative splicing by inducing localized histone hyperacetylation in an RNA-dependent manner. *Proc. Natl. Acad. Sci.* **108**, E627–E635 (2011).

50. Han, H.-J., Russo, J., Kohwi, Y. & Kohwi-Shigematsu, T. SATB1 reprogrammes gene expression to promote breast tumour growth and metastasis. *Nature* **452**, 187–193 (2008).

51. Corces, M. R. *et al.* The chromatin accessibility landscape of primary human cancers. *Science* **362**, eaav1898 (2018).

52. Guo, L. *et al.* Nuclear-import receptors reverse aberrant phase transitions of RNA-binding proteins with prion-like domains. *Cell* **173**, 677-692.e20 (2018).

53. Yoshizawa, T. *et al.* Nuclear import receptor inhibits phase separation of FUS through binding to multiple sites. *Cell* **173**, 693-705.e22 (2018).

54. Nakayama, Y., Mian, I. S., Kohwi-Shigematsu, T. & Ogawa, T. A nuclear targeting determinant for SATB1, a genome organizer in the T cell lineage. *Cell Cycle* **4**, 1099–1106 (2005).

55. Kumar, P. P. *et al.* Functional interaction between PML and SATB1 regulates chromatin-loop architecture and transcription of the MHC class I locus. *Nat. Cell Biol.* **9**, 45–56 (2007).

56. Banani, S. F. *et al.* Compositional control of phase-separated cellular bodies. *Cell* **166**, 651–663 (2016).

57. Tan, J.-A. T., Song, J., Chen, Y. & Durrin, L. K. Phosphorylation-dependent interaction of SATB1 and PIAS1 directs SUMO-regulated caspase cleavage of SATB1. *Mol. Cell. Biol.* **30**, 2823–2836 (2010).

58. Cai, D. *et al.* Phase separation of YAP reorganizes genome topology for long-term YAP target gene expression. *Nat. Cell Biol.* **21**, 1578–1589 (2019).

59. Lu, Y. *et al.* Phase separation of TAZ compartmentalizes the transcription machinery to promote gene expression. *Nat. Cell Biol.* **22**, 453–464 (2020).

60. Zamudio, A. V. *et al.* Mediator condensates localize signaling factors to key cell identity genes. *Mol. Cell* **76**, 753-766.e6 (2019).

61. Durślewicz, J. *et al.* Prognostic significance of TLR2, SMAD3 and localization-dependent SATB1 in stage I and II non–small-cell lung cancer patients. *Cancer Control* **28**, 10732748211056696 (2021).

62. Gruber, A. *et al.* Molecular and structural architecture of polyQ aggregates in yeast. *Proc. Natl. Acad. Sci.* **115**, E3446–E3453 (2018).

63. Kim, D., Paggi, J. M., Park, C., Bennett, C. & Salzberg, S. L. Graph-based genome alignment and genotyping with HISAT2 and HISAT-genotype. *Nat. Biotechnol.* **37**, 907–915 (2019).

64. Pertea, M. *et al.* StringTie enables improved reconstruction of a transcriptome from RNA-seq reads. *Nat. Biotechnol.* **33**, 290–295 (2015).

65. Liao, Y., Smyth, G. K. & Shi, W. featureCounts: an efficient general purpose program for assigning sequence reads to genomic features. *Bioinformatics* **30**, 923–930 (2014).

66. Love, M. I., Huber, W. & Anders, S. Moderated estimation of fold change and dispersion for RNA-seq data with DESeq2. *Genome Biol.* **15**, 550 (2014).

67. Zhang, Y. *et al.* Model-based analysis of ChIP-Seq (MACS). *Genome Biol.* **9**, R137 (2008).

68. Sterne-Weiler, T., Weatheritt, R. J., Best, A. J., Ha, K. C. H. & Blencowe, B. J. Efficient and accurate quantitative profiling of alternative splicing patterns of any complexity on a laptop. *Mol. Cell* **72**, 187-200.e6 (2018).

69. Stratigi, K. *et al.* Spatial proximity of homologous alleles and long noncoding RNAs regulate a switch in allelic gene expression. *Proc. Natl. Acad. Sci.* **112**, E1577–E1586 (2015).

70. Szklarczyk, D. *et al.* STRING v11: protein–protein association networks with increased coverage, supporting functional discovery in genome-wide experimental datasets. *Nucleic Acids Res.* **47**, D607–D613 (2019).

71. Hagberg, A., Swart, P. & S Chult, D. *Exploring network structure, dynamics, and function using networkx*. https://www.osti.gov/biblio/960616-exploring-network-structure-dynamics-function-using-networkx (2008).

72. Grover, A. & Leskovec, J. node2vec: scalable feature learning for networks. in *Proceedings of the 22nd ACM SIGKDD International Conference on Knowledge Discovery and Data Mining* 855–864 (ACM, 2016). doi:10.1145/2939672.2939754.

73. Raudvere, U. *et al.* g:Profiler: a web server for functional enrichment analysis and conversions of gene lists (2019 update). *Nucleic Acids Res.* **47**, W191–W198 (2019).

74. Yaneva, M. & Tempst, P. Affinity capture of specific DNA-binding proteins for mass spectrometric identification. *Anal. Chem.* **75**, 6437–6448 (2003).

75. Yaneva, M. & Tempst, P. Isolation and mass spectrometry of specific DNA binding proteins. *Methods Mol. Biol. Clifton NJ* **338**, 291–303 (2006).

76. Spilianakis, C. G., Lalioti, M. D., Town, T., Lee, G. R. & Flavell, R. A. Interchromosomal associations between alternatively expressed loci. *Nature* **435**, 637–645 (2005).

77. Williams, A. *et al.* Hypersensitive site 6 of the Th2 locus control region is essential for Th2 cytokine expression. *Proc. Natl. Acad. Sci. U. S. A.* **110**, 6955–6960 (2013).

78. Schindelin, J. *et al.* Fiji: an open-source platform for biological-image analysis. *Nat. Methods* **9**, 676–682 (2012).

79. Candeloro, P. *et al.* Raman database of amino acids solutions: a critical study of Extended Multiplicative Signal Correction. *Analyst* **138**, 7331–7340 (2013).

80. Thévenaz, P., Ruttimann, U. E. & Unser, M. A pyramid approach to subpixel registration based on intensity. *IEEE Trans. Image Process. Publ. IEEE Signal Process. Soc.* **7**, 27–41 (1998).

81. Lancaster, A. K., Nutter-Upham, A., Lindquist, S. & King, O. D. PLAAC: a web and command-line application to identify proteins with prion-like amino acid composition. *Bioinformatics* **30**, 2501–2502 (2014).

82. Ramírez, F. *et al.* deepTools2: a next generation web server for deep-sequencing data analysis. *Nucleic Acids Res.* **44**, W160-165 (2016).

83. Morganella, S., Pagnotta, S. M. & Ceccarelli, M. Finding recurrent copy number alterations preserving within-sample homogeneity. *Bioinforma. Oxf. Engl.* **27**, 2949–2956 (2011).

84. Lawrence, M. *et al.* Software for computing and annotating genomic ranges. *PLoS Comput. Biol.* **9**, e1003118 (2013).

85. Therneau, T. M. & Grambsch, P. M. *Modeling survival data: extending the Cox model*. (Springer, 2000).

86. Costes, S. V. *et al.* Automatic and quantitative measurement of protein-protein colocalization in live cells. *Biophys. J.* **86**, 3993–4003 (2004).

Figure legends

Fig. 1 | Identification of two SATB1 protein isoforms in murine thymocytes.

a, SATB1 protein consists of the following domains and structural features: ULD – ubiquitin-like domain, CUTL – CUT-like domain, CUT1 and CUT2 domains, EP – the peptide encoded by the predicted extra exon of the long *Satb1* isoform, Q – compositional bias represented by a poly-Q domain and a stretch of prolines, HD – homeodomain. In this study, we used two custom-made antibodies (Davids Biotechnology): an antibody targeting the first 330 amino acids of all isoforms (cannot discriminate between the two protein isoforms) and the long isoform antibody specifically targeting the extra peptide of the long isoform. **b**, Comprehensive list of quantified *Satb1* isoforms based on stranded-total-RNA-seq experiment in thymocytes. Data are the mean ± s.d. **c**, Design of the RT-qPCR experiment to quantitate relative expression of the short and long *Satb1* isoforms in murine thymocytes. **d**, RT-qPCR results for the relative mRNA levels of the two *Satb1* isoforms. Values from different replicates were normalized to *Dnmt1* mRNA levels. Data are the mean ± s.d. **e**, Scheme for the approach utilized to detect SATB1 long isoform and validate the custom-made long isoform-specific antibody (Davids Biotechnology). Whole cell thymocyte protein extracts (sample 1) were prepared and incubated with a custom-made antibody against the long SATB1 isoform. The immunoprecipitated material (sample 2) was kept and the immunodepleted material was subjected on a second immunoprecipitation reaction utilizing an antibody detecting epitopes on both long and short SATB1 isoforms (Santa Cruz Biotechnology, sc-376096). The material from the second immunoprecipitation reaction was kept (sample 3), as well as the immunodepleted thymocyte extract for all SATB1 isoforms (sample 4). **f**, Western blot analysis for the samples described in **e**. The whole thymocyte protein extract (1), immunoprecipitated long SATB1 protein (2), immunoprecipitated short SATB1 protein (3) and total thymocyte protein fraction

immunodepleted for both SATB1 isoforms (4). UPPER PANEL: Western blot analysis utilizing a SATB1 antibody detecting only the long SATB1 isoform. LOWER PANEL: Western blot analysis utilizing a SATB1 antibody detecting all SATB1 isoforms. **f**, Confocal and STED microscopy images indicating the subnuclear SATB1 cage-like pattern. The super-resolution microscopy unveils that the cage-like pattern is actually composed of individual, mostly round, 40-60 nm large speckles.

Fig. 2 | SATB1 is localized in the active nuclear zone and sites of active transcription.

a, 3D-SIM immunofluorescence experiment utilizing two different SATB1 antibodies to visualize the nuclear localization pattern of the long isoform compared to all SATB1 isoforms. Scale bar 2 µm. **b**, Quantification of the 3D-SIM immunofluorescence images. Nuclei of primary murine thymocytes were categorized into four zones based on the intensity of DAPI staining and SATB1 speckles in each zone were counted. Images used represented a middle z-stack from the 3D-SIM experiments. The graph depicts the differences between long and all SATB1 isoforms' zonal localization in the nucleus. The horizontal lines inside violin plots represent the 25th, 50th and 75th percentiles. Red circles represent the mean ± s.d. *P* values by Wilcoxon rank sum test. **c**, STED microscopy indicating that SATB1 speckles co-localize with sites of active transcription (60 minutes pulse 5-fluorouridine treatment). Scale bar 1 µm. **d**, STRING network of all significantly enriched SATB1-interacting proteins clustered using the k-means method (left). The full network, including protein names, is available in Supplementary Fig. 2c. The blue cluster 1 and yellow cluster 2 were enriched for transcription and splicing-related factors, respectively. A more detailed network of selected transcription and splicing-related factors is provided (right). **e**, Gene ontology enrichment analysis of SATB1-interacting proteins revealed factors involved in transcription and

splicing. **f**, Volcano plot from stranded-total-RNA-seq experiment displaying the differentially expressed genes (FDR < 0.05) in *Satb1* cKO thymocytes.

Fig. 3 | SATB1 forms phase separated droplets *in vivo*.

a, 3D-SIM immunofluorescence microscopy on 1,6-hexanediol-treated cells. Increasing concentration of 1,6-hexanediol gradually solubilized long SATB1 isoform speckles. **b**, Quantification of results in **a** showing a gradual decrease of SATB1 signal, indicating its sensitivity to 1,6-hexanediol treatment. **c**, Comparison of immunofluorescence signal based on the antibody targeting all the SATB1 isoforms (Santa Cruz Biotechnology, sc-5990) and only the long isoform (Davids Biotechnology, custom-made) upon 1,6-hexanediol treatment, detected by STED microscopy. **d**, Colocalization of SATB1 and fluorouridine-stained sites of active transcription (inset visualized in Fig. 2c) and its deregulation upon 10% 1,6-hexanediol treatment. **e**, LEFT: Pearson correlation coefficients (PCC) derived from pixel-based colocalization analysis between long and/or all SATB1 isoforms and fluorouridine-stained sites of active transcription, with and without 10% 1,6-hexanediol treatment. RIGHT: the Costes P-values[86] derived from randomly shuffled chunks of analyzed images (100 randomizations). The grey line indicates a 0.95 level of significance. Images used for the analysis were generated by STED microscopy. Complete results of the colocalization analysis for both STED and 3D-SIM experiments, including Manders‘ coefficients are depicted in Supplementary Fig. 3a-c. **f**, Principal component analysis of Raman spectra from WT and *Satb1* cKO thymocytes with and without 10% 1,6-hexanediol treatment. In **b**, **c** and **e**, the horizontal lines inside violin plots represent the 25th, 50th and 75th percentile. Red circles represent the mean ± s.d. *P* values by Wilcoxon rank sum test.

Fig. 4 | The N-terminus of SATB1 forms phase separated droplets.

a, Graphical representation of all CRY2-mCherry constructs generated. The graph displays the IDR prediction by VL3 PONDR score in magenta and the prediction of prion-like domains by PLAAC algorithm in green. **b**, Formation of optoDroplets upon 488 nm pulse illumination in live cells transiently transfected with CRY2-mCherry-N-terminus_SATB1 constructs as well as with negative (vector) and positive control constructs (N-terminal part of FUS protein). Two groups of cells were identified based on the original relative expression levels of the recombinant proteins. Scale bar 5 µm. **c**, OptoDroplets evinced a round shape and the ability to coalesce. **d**, Number of optoDroplets normalized to the cell size at each time point upon activation, to visualize the speed of droplet assembly and its dependence on the original concentration of the protein. **e**, Number of optoDroplets normalized to the cell size at each time point of inactivation (488 nm laser was off) to visualize the speed of droplet disassembly and its dependence on the original concentration of the protein. **f**, FRAP experiment utilizing either the N-terminus of SATB1 construct or the FUS positive control construct. The fitted curves were generated by the exponential recovery curve fitting function of Fiji. In **d**, **e** and **f**, the error bars represent the s.e.m.

Fig. 5 | Discrete biophysical properties of SATB1 protein isoforms.

a, CRY2-mCherry constructs expressing both the short and the long full length SATB1 isoforms underwent reversible ultrastructural changes. Scale bar 5 µm. **b**, In a fraction of cells, the full-length long SATB1 isoform was mislocalized outside the nucleus which triggered the formation of irreversible aggregates. Scale bar 5 µm. **c**, Comparison of LLPS propensity predicted by the *cat*GRANULE[37] algorithm of human (Q01826-1 and Q01826-2, for short and long isoform, respectively; UniProtKB) and murine (Q60611 and E9PVB7, for short and long isoform, respectively; UniProtKB) SATB1 protein isoforms. Human long SATB1 isoform displays higher phase separation propensity compared to murine protein. Both long SATB1 isoforms have an

increased propensity to undergo phase separation compared to short isoforms due to the presence of the extra peptide with a compositional bias (enrichment in S, G, Q, P, E, K and R amino acids in the murine SATB1). **d**, CRY2-mCherry constructs encompassing only the two SATB1 IDR regions and the poly-Q domain, but not the NLS signal, displayed much higher rates of cytoplasmic aggregation for the long SATB1 isoform compared to the short isoform. Green arrows indicate cells with long SATB1 isoform aggregates.

Fig. 6 | Modes of regulation of SATB1 phase transitions.

a, Nuclear matrix extraction coupled to immunofluorescence analysis revealed that a fraction of SATB1 protein (Santa Cruz Biotechnology, sc-5990) remained in the cell nucleus even after DNase I treatment and high-salt extraction. However, RNase A treatment almost completely depleted SATB1 from the nucleus, indicating a high level of association between SATB1 and nuclear RNA. **b**, SATB1 co-immunoprecipitation confirmed the association of SATB1 with lncRNA Xist. Black dots represent individual % input measurements for Xist RIP (3 biological replicates, 4 Xist regions targeted) and control RIP experiments (3 biological replicates; 3 control RNAs: *Tbp*, *Smc1a*, Dxz4). The horizontal lines inside violin plots represent the 25th, 50th and 75th percentiles. Red circle represents the mean ± s.d. Mean fold enrichment for Xist RIP is 36 ± 20 s.d. **c**, Forced nuclear localization of CRY2-mCherry constructs harboring the long SATB1 isoform IDR and the SV40 NLS displayed no protein association in response to 488 nm laser even after 20 minutes of activation. Scale bar 5 μm. **d**, The S635A mutation, preventing phosphorylation of the short SATB1 isoform highly increased the aggregation propensity of the corresponding CRY2-mCherry-IDR construct. Green arrows indicate cells with the SATB1 aggregates. **e**, Murine *Satb1* transcripts reconstructed based on stranded-total-RNA-seq data. Both long and short *Satb1* isoforms were produced from multiple promoters. The long SATB1 isoform binding sites were retrieved from

GSE173446[19]. **f**, Increased ATAC-seq signal in human breast cancer patients is positively correlated with the expression of the short *SATB1* isoform and negatively correlated with the long isoform expression. **g**, In human breast cancer patients, high pathological T categories (indicating bigger extent of the primary tumor, presumably indicating worse prognosis; labeling based on the TNM cancer staging system) were associated with higher expression of the long *SATB1* isoform. In contrast, the expression of the short *SATB1* isoform was negatively correlated with the pathological T categories. Median RNA expression values for both isoforms based on all transcripts with non-zero expression values are displayed. Red circles represent the median values.

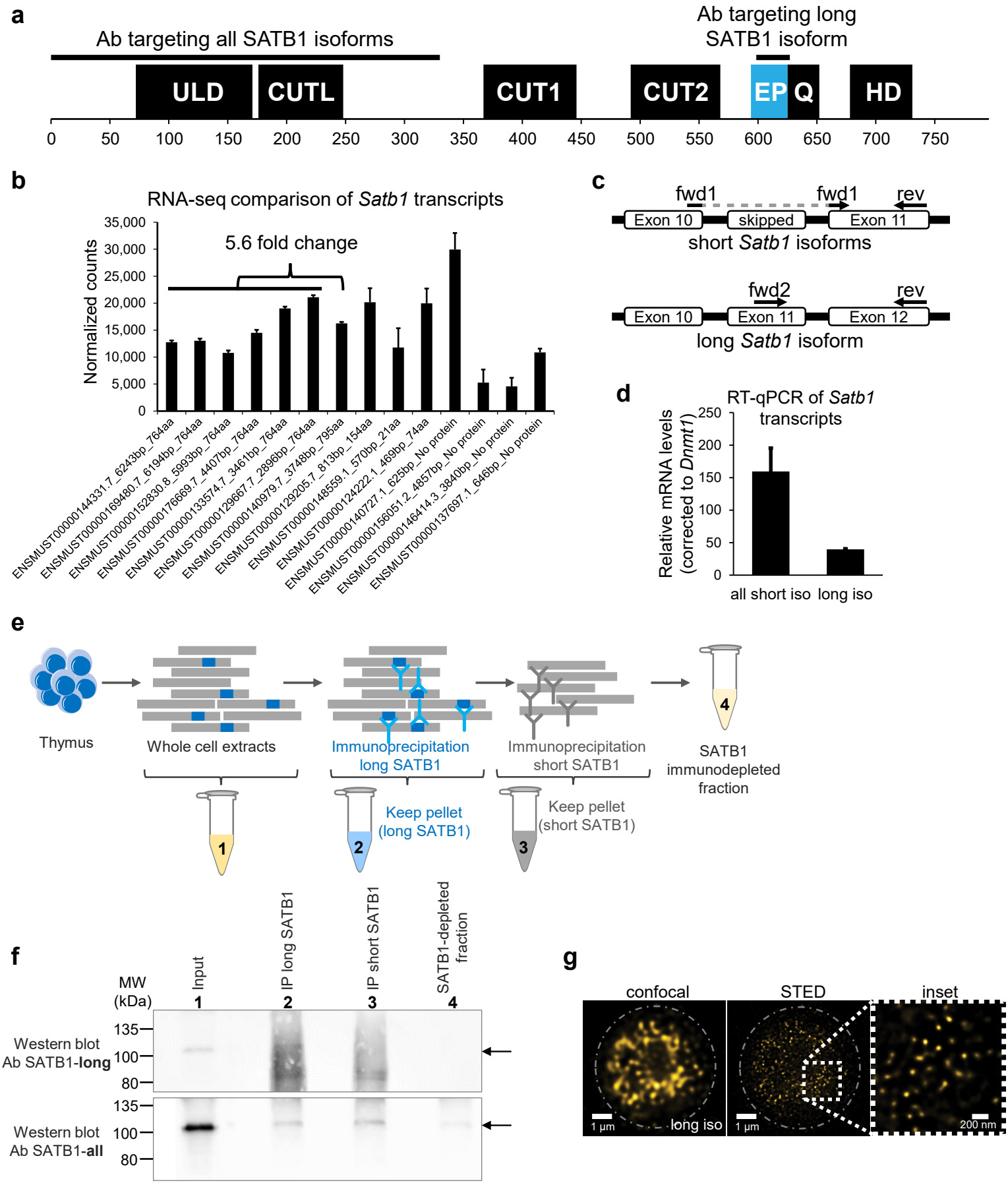
a
Ab targeting all SATB1 isoforms
Ab targeting long SATB1 isoform
ULD
CUTL
CUT1
CUT2
EP
Q
HD
0 50 100 150 200 250 300 350 400 450 500 550 600 650 700 750
b
RNA-seq comparison of Satb1 transcripts
5.6 fold change
Normalized counts
35,000 30,000 25,000 20,000 15,000 10,000 5,000 0
ENSMUST00000144331.7_6243bp_764aa
ENSMUST00000169480.7_6194bp_764aa
ENSMUST00000152830.8_5993bp_764aa
ENSMUST00000176669.7_4407bp_764aa
ENSMUST00000133574.7_3461bp_764aa
ENSMUST00000129667.7_2896bp_764aa
ENSMUST00000140979.7_3748bp_795aa
ENSMUST00000129205.7_813bp_154aa
ENSMUST00000148559.1_570bp_21aa
ENSMUST00000124222.1_469bp_74aa
ENSMUST00000140727.1_625bp_No protein
ENSMUST00000156051.2_4857bp_No protein
ENSMUST00000146414.3_3840bp_No protein
ENSMUST00000137697.1_646bp_No protein
c
fwd1
fwd1
rev
Exon 10
skipped
Exon 11
short Satb1 isoforms
fwd2
rev
Exon 10
Exon 11
Exon 12
long Satb1 isoform
d
RT-qPCR of Satb1 transcripts
Relative mRNA levels (corrected to Dnmt1)
250 200 150 100 50 0
all short iso
long iso
e
Thymus
Whole cell extracts
Immunoprecipitation long SATB1
Immunoprecipitation short SATB1
SATB1 immunodepleted fraction
1
2
Keep pellet (long SATB1)
3
Keep pellet (short SATB1)
4
f
MW (kDa)
Input 1
IP long SATB1 2
IP short SATB1 3
SATB1-depleted fraction 4
Western blot Ab SATB1-long
135 100 80
Western blot Ab SATB1-all
135 100 80
g
confocal
STED
inset
1 µm
long iso
1 µm
200 nm

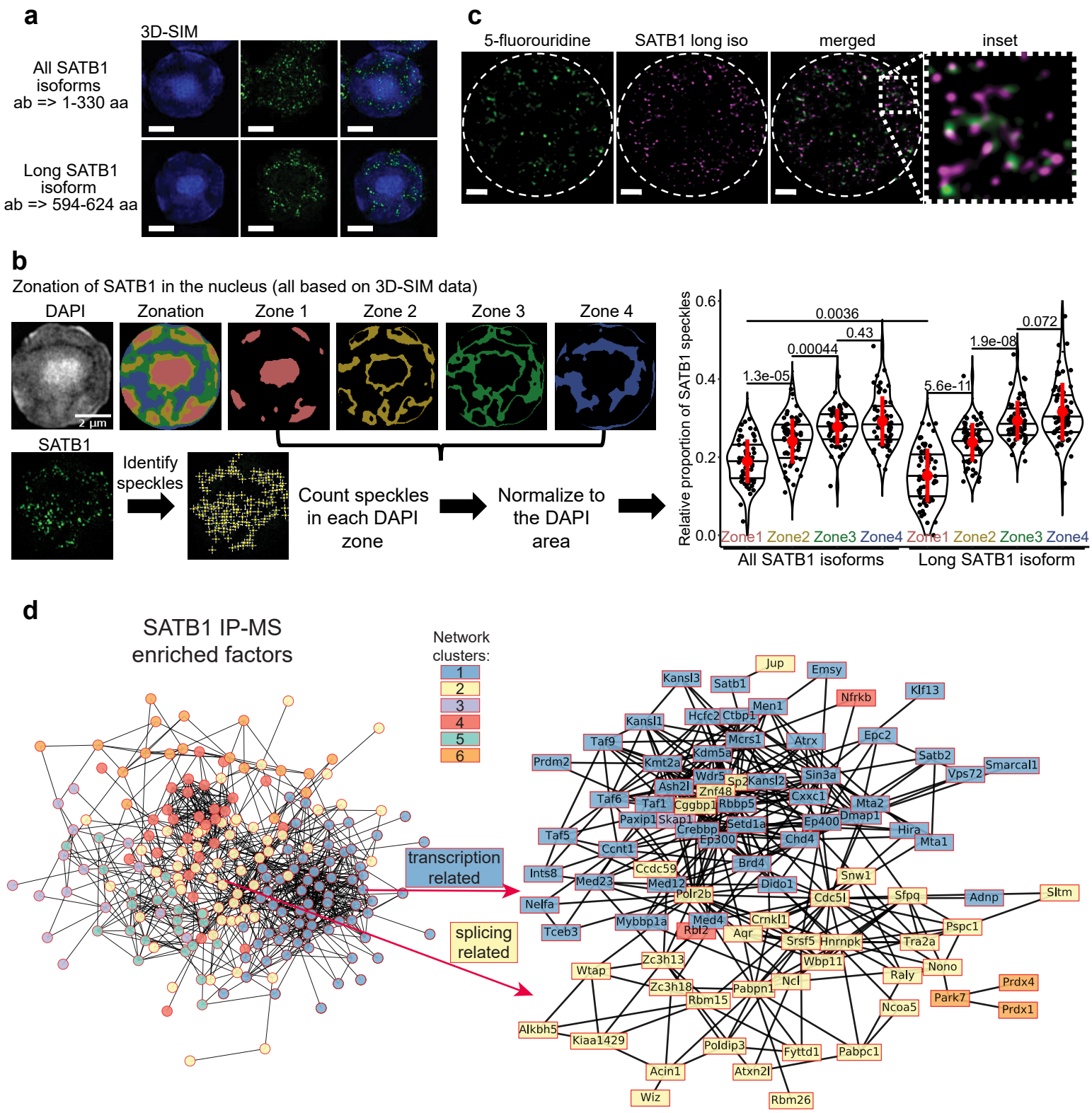
a
3D-SIM
All SATB1 isoforms ab => 1-330 aa
Long SATB1 isoform ab => 594-624 aa
c
5-fluorouridine
SATB1 long iso
merged
inset
b
Zonation of SATB1 in the nucleus (all based on 3D-SIM data)
DAPI
Zonation
Zone 1
Zone 2
Zone 3
Zone 4
2 µm
SATB1
Identify speckles
Count speckles in each DAPI zone
Normalize to the DAPI area
Relative proportion of SATB1 speckles
0.0036
0.43
0.00044
1.3e-05
5.6e-11
1.9e-08
0.072
Zone1 Zone2 Zone3 Zone4 Zone1 Zone2 Zone3 Zone4
All SATB1 isoforms
Long SATB1 isoform
d
SATB1 IP-MS enriched factors
Network clusters:
1
2
3
4
5
6
transcription related
splicing related
e
GO - Biological process
mRNA splicing, via spliceosome
15 (2.0e-04)
Transcription by RNA polymerase II
57 (9.3e-08)
Gene expression
120 (5.5e-19)
Histone modification
39 (9.8e-23)
Number of proteins matched (adj. p-value)
f
RNA sequencing
922 DOWN
719 UP
-log10 (p-value)
log2 (fold change)

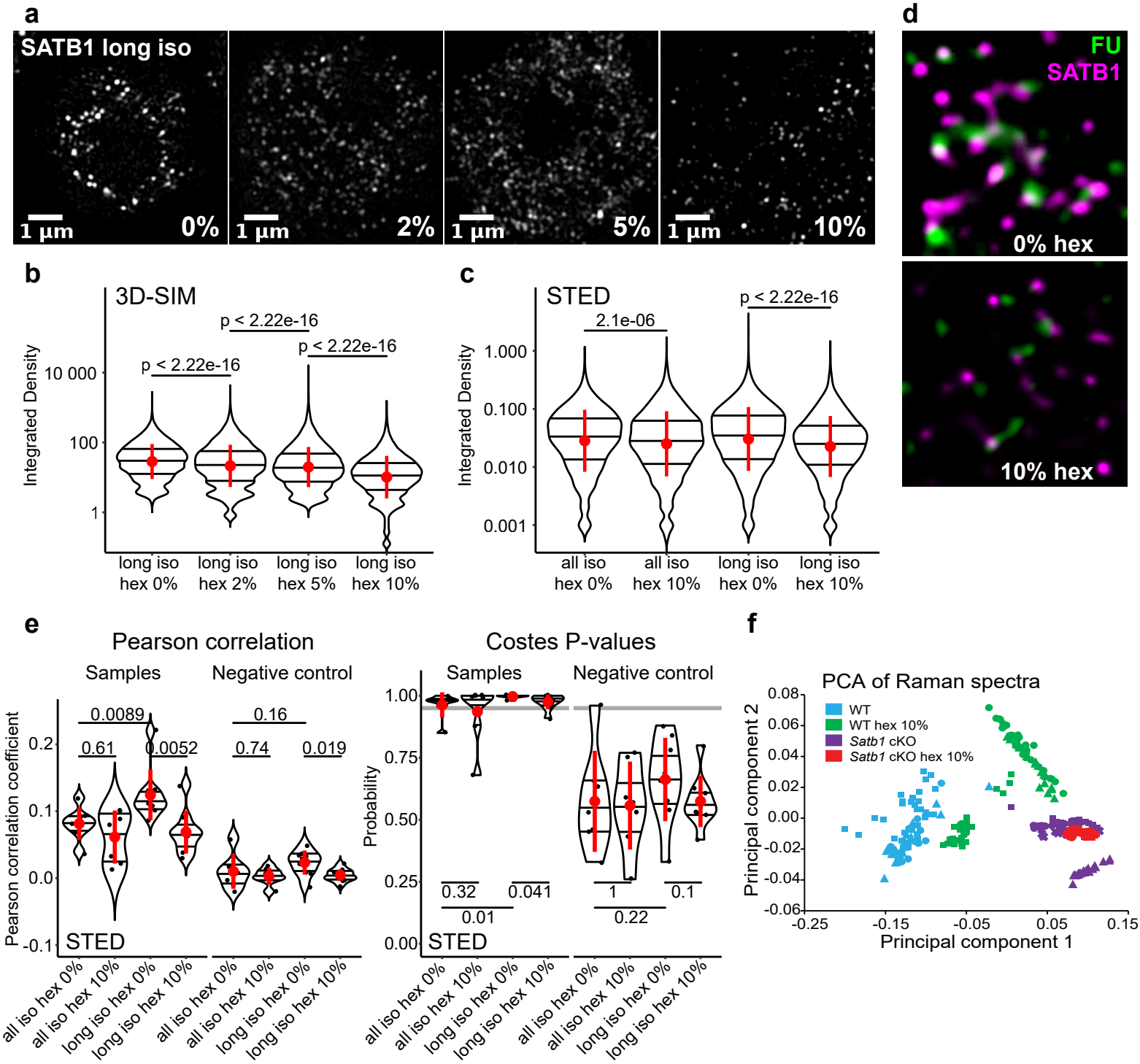
a
SATB1 long iso
1 µm
0%
2%
5%
10%
d
FU
SATB1
0% hex
10% hex
b
3D-SIM
Integrated Density
10 000
100
1
p < 2.22e-16
p < 2.22e-16
p < 2.22e-16
long iso hex 0%
long iso hex 2%
long iso hex 5%
long iso hex 10%
c
STED
Integrated Density
1.000
0.100
0.010
0.001
2.1e-06
p < 2.22e-16
all iso hex 0%
all iso hex 10%
long iso hex 0%
long iso hex 10%
e
Pearson correlation
Samples
Negative control
Pearson correlation coefficient
0.2
0.1
0.0
-0.1
0.0089
0.61
0.0052
0.16
0.74
0.019
STED
all iso hex 0%
all iso hex 10%
long iso hex 0%
long iso hex 10%
Costes P-values
Samples
Negative control
Probability
1.00
0.75
0.50
0.25
0.00
0.32
0.041
0.01
1
0.1
0.22
STED
f
PCA of Raman spectra
WT
WT hex 10%
Satb1 cKO
Satb1 cKO hex 10%
Principal component 2
0.08
0.06
0.04
0.02
0.00
-0.02
-0.04
-0.06
-0.25
-0.15
-0.05
0.05
0.15
Principal component 1

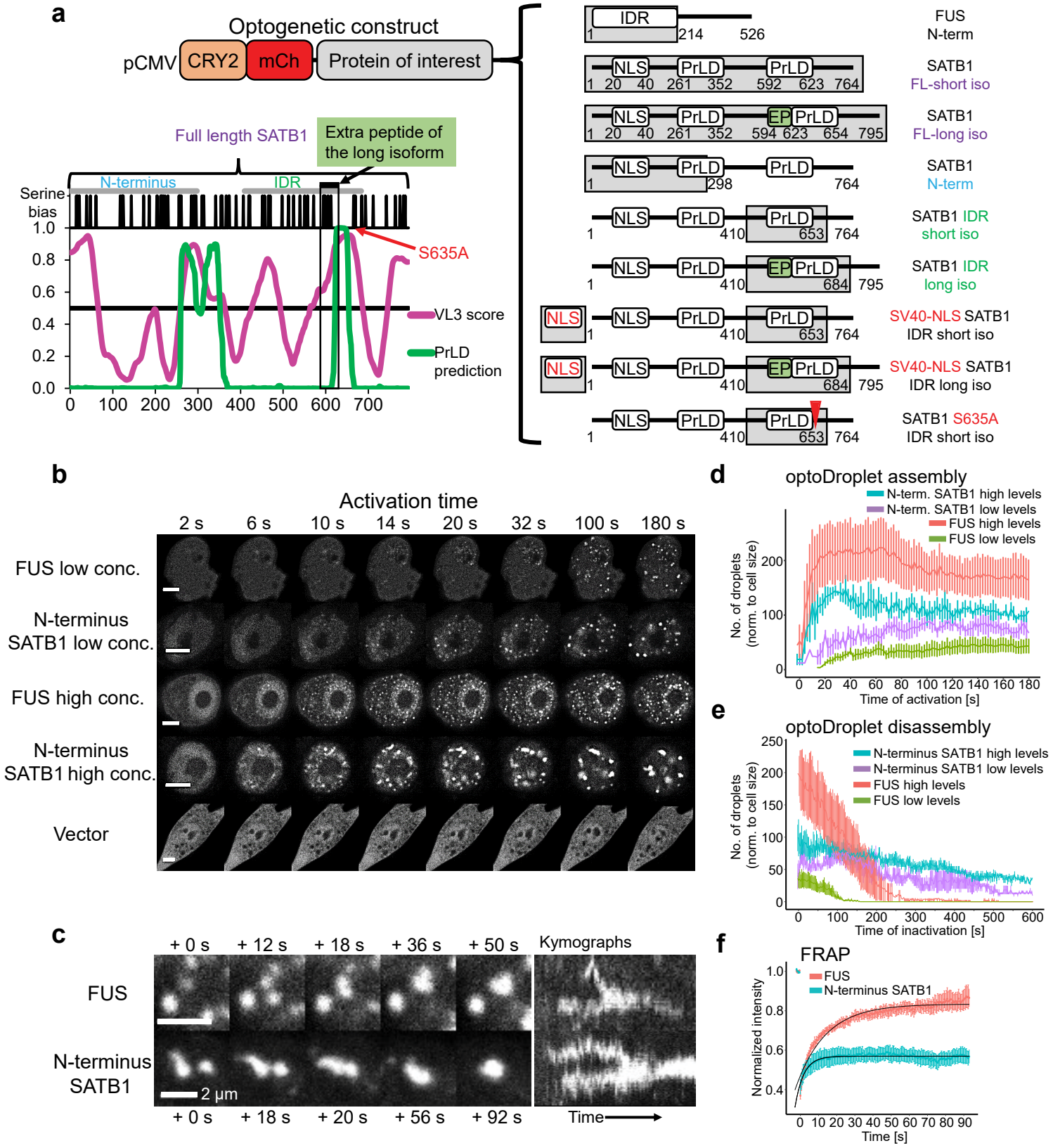
a
Optogenetic construct
pCMV
CRY2
mCh
Protein of interest
Full length SATB1
Extra peptide of the long isoform
N-terminus
IDR
Serine bias
S635A
VL3 score
PrLD prediction
IDR
FUS N-term
NLS
PrLD
SATB1 FL-short iso
EP
SATB1 FL-long iso
SATB1 N-term
SATB1 IDR short iso
SATB1 IDR long iso
SV40-NLS SATB1 IDR short iso
SV40-NLS SATB1 IDR long iso
SATB1 S635A IDR short iso
b
Activation time
FUS low conc.
N-terminus SATB1 low conc.
FUS high conc.
N-terminus SATB1 high conc.
Vector
c
FUS
N-terminus SATB1
Kymographs
2 µm
Time
d
optoDroplet assembly
N-term. SATB1 high levels
N-term. SATB1 low levels
FUS high levels
FUS low levels
No. of droplets (norm. to cell size)
Time of activation [s]
e
optoDroplet disassembly
N-terminus SATB1 high levels
N-terminus SATB1 low levels
FUS high levels
FUS low levels
Time of inactivation [s]
f
FRAP
FUS
N-terminus SATB1
Normalized intensity
Time [s]

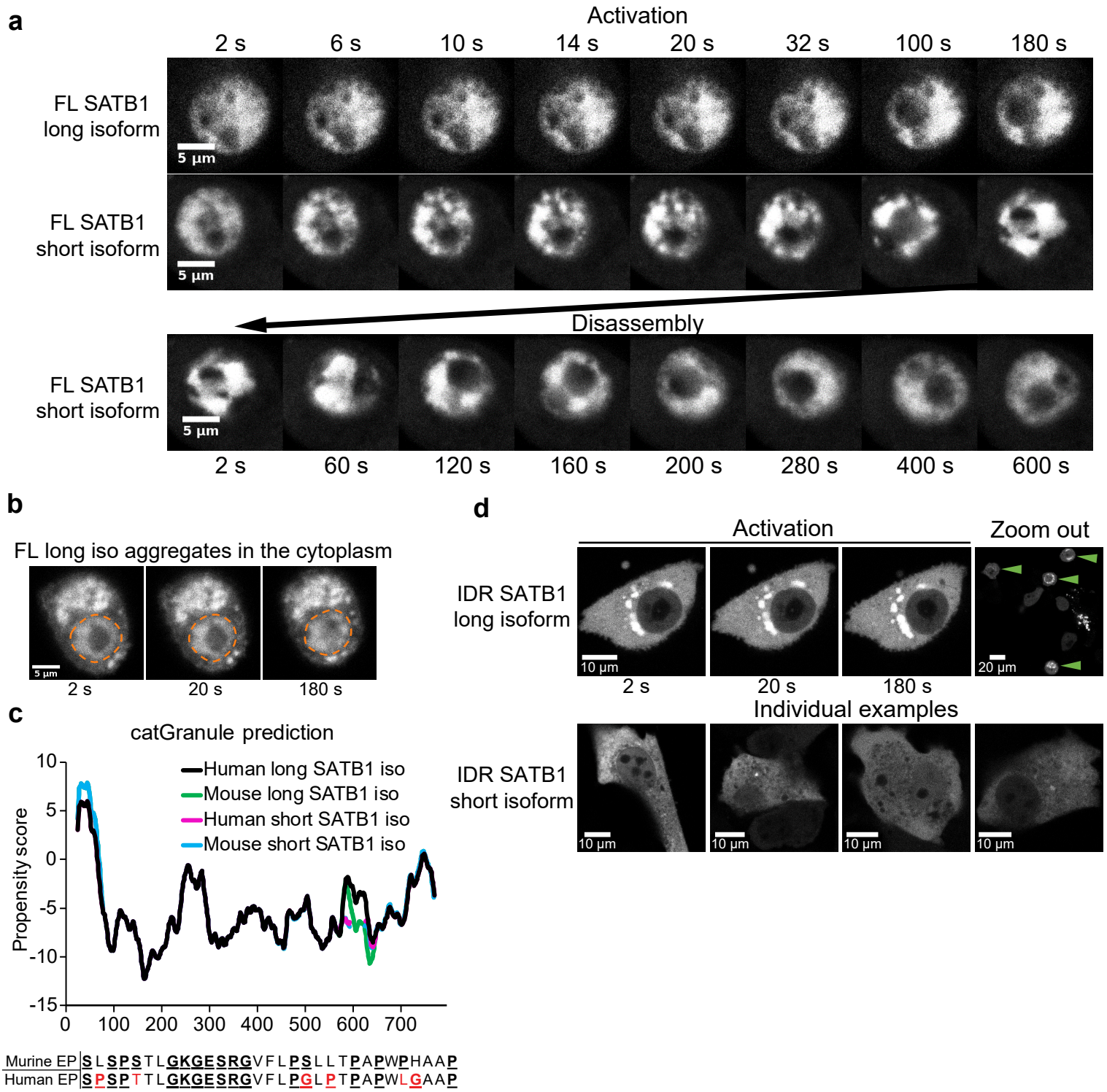
a
Activation
2 s
6 s
10 s
14 s
20 s
32 s
100 s
180 s
FL SATB1
long isoform
5 µm
FL SATB1
short isoform
5 µm
Disassembly
FL SATB1
short isoform
5 µm
2 s
60 s
120 s
160 s
200 s
280 s
400 s
600 s
b
FL long iso aggregates in the cytoplasm
5 µm
2 s
20 s
180 s
c
catGranule prediction
Human long SATB1 iso
Mouse long SATB1 iso
Human short SATB1 iso
Mouse short SATB1 iso
Propensity score
10
5
0
-5
-10
-15
0
100
200
300
400
500
600
700
Murine EP SLSPSTLGKGESRGVFLPSLLTPAPWPHAAP
Human EP SPSPTTLGKGESRGVFLPGLPTPAPWLGAAP
d
Activation
Zoom out
IDR SATB1
long isoform
10 µm
20 µm
2 s
20 s
180 s
Individual examples
IDR SATB1
short isoform
10 µm
10 µm
10 µm
10 µm

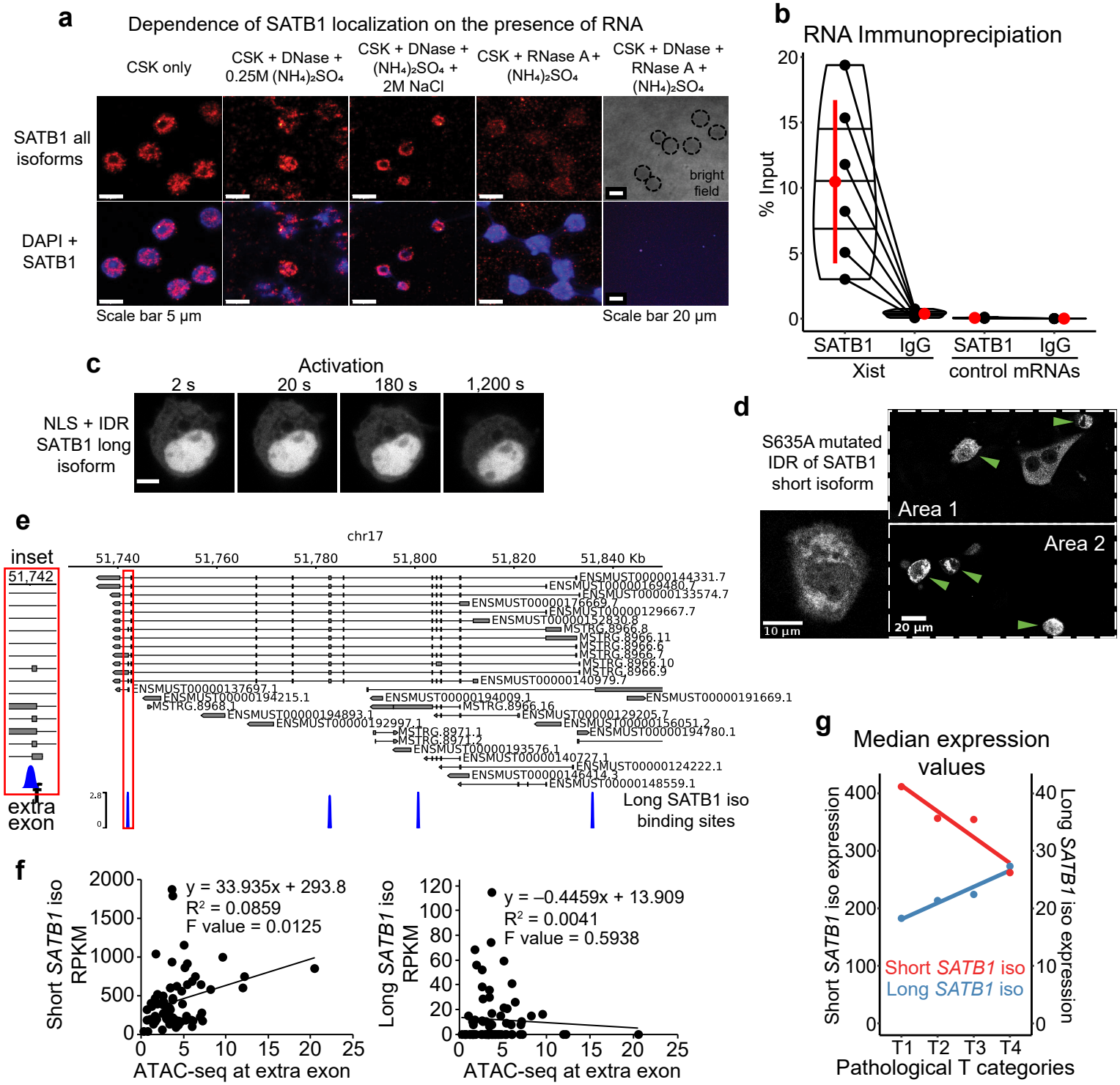
a
Dependence of SATB1 localization on the presence of RNA
CSK only
CSK + DNase + 0.25M (NH₄)₂SO₄
CSK + DNase + (NH₄)₂SO₄ + 2M NaCl
CSK + RNase A + (NH₄)₂SO₄
CSK + DNase + RNase A + (NH₄)₂SO₄
SATB1 all isoforms
DAPI + SATB1
bright field
Scale bar 5 µm
Scale bar 20 µm
b
RNA Immunoprecipiation
% Input
SATB1
IgG
Xist
control mRNAs
c
Activation
2 s
20 s
180 s
1,200 s
NLS + IDR SATB1 long isoform
d
S635A mutated IDR of SATB1 short isoform
Area 1
Area 2
10 µm
20 µm
e
chr17
inset
51,742
51,740
51,760
51,780
51,800
51,820
51,840 Kb
extra exon
Long SATB1 iso binding sites
f
y = 33.935x + 293.8
R² = 0.0859
F value = 0.0125
Short SATB1 iso RPKM
ATAC-seq at extra exon
y = –0.4459x + 13.909
R² = 0.0041
F value = 0.5938
Long SATB1 iso RPKM
ATAC-seq at extra exon
g
Median expression values
Short SATB1 iso expression
Long SATB1 iso expression
Short SATB1 iso
Long SATB1 iso
T1
T2
T3
T4
Pathological T categories